Sustainable Cities and Society 114 (2024) 105733

Contents lists available at ScienceDirect

Sustainable Cities and Society

journal homepage: www.elsevier.com/locate/scs

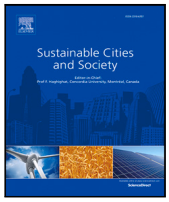

Microclimate Vision: Multimodal prediction of climatic parameters using street-level and satellite imagery

Kunihiko Fujiwara [a,b], Maxim Khomiakov [c], Winston Yap [a], Marcel Ignatius [a], Filip Biljecki [a,d,*]

[a] Department of Architecture, National University of Singapore, Singapore
[b] Research & Development Institute, Takenaka Corporation, Japan
[c] Department of Applied Mathematics and Computer Science, Technical University of Denmark, Denmark
[d] Department of Real Estate, National University of Singapore, Singapore

ARTICLE INFO

Keywords:
Urban thermal environment
Heat risk management
Climate change adaptation
Urban morphology
Street-view imagery
Computer vision
Solar radiation

ABSTRACT

High-resolution microclimate data is essential for capturing spatio-temporal heterogeneity of urban climate and heat health management. However, previous studies have relied on dense measurements that require significant costs for equipment, or on physical simulations demanding intensive computational loads. As a potential alternative to these methods, we propose a multimodal deep learning model to predict microclimate at a high spatial and temporal resolution based on street-level and satellite imagery. This model consists of LSTM and ResNet-18 architectures, and predicts air temperature (T_{air}), relative humidity (RH), wind speed (v), and global horizontal irradiance (GHI). For our study area situated at a university campus in Singapore, we collected microclimate data, street-level and satellite imagery. We conducted extensive experiments with our collected dataset to showcase our model's predictive capabilities and its practical use in generating high-resolution microclimate maps. Our model reported RMSE at 0.95 °C for T_{air}, 2.57% for RH, 0.31 m/s for v, and 225 W/m^2 for GHI. Furthermore, we observed a contribution of imagery inputs to higher accuracy by comparing models with and without such inputs. We identified hot spots at a high spatio-temporal resolution, indicating its application for issuing real-time heat alerts. Our models are released openly at the microclimate-vision GitHub repository (https://github.com/kunifujiwara/microclimate-vision).

1. Introduction

The increasing attention to urban microclimate is largely driven by concerns about climate change (Xiao & Yuizono, 2022), heat waves (Kotharkar & Ghosh, 2022; Li et al., 2023; Taleghani et al., 2019), and the heat island effect associated with urbanization (Kousis et al., 2022). Concurrently, there is a growing interest in aspects of walkability (Azegami et al., 2023; Saadi et al., 2021; Shartova et al., 2023), bikeability (Arellana et al., 2020; Ito & Biljecki, 2021; Wang, Jin et al., 2024), and resulting health and well-being (Pedersen Zari et al., 2022; Reyes-Riveros et al., 2021), which further emphasizes the importance of urban microclimate in fostering sustainable cities. To mitigate microclimate-related risk and improve the health and well-being of city dwellers, it is important for policymakers and urban planners to monitor microclimate, and assess and manage the risk properly (Gaspari & Fabbri, 2017; Hamdan & de Oliveira, 2019). Against this context, our study focuses on heat risk, which is of growing concern amid global warming. However, it is important to note that microclimate-related risks encompass not only heat but also cold and wind hazards.

The four principal microclimate parameters — air temperature, relative humidity, wind speed, and radiation — play a critical role in determining heat stress and risk (Kumar & Sharma, 2020). These microclimate parameters are significantly influenced by surrounding urban morphological features such as building density and the amount of vegetation, and ground surface materials (Zhao et al., 2018). Consequently, the microclimate can vary substantially within areas at microscale, depending on the heterogeneity in these features (Chàfer et al., 2022; Jin et al., 2018; Kousis et al., 2022, 2021). Failing to capture such variances may degrade the performance of downstream applications. Additionally, the trend of spatial heterogeneity of microclimate can vary over time. This spatial and temporal variability of microclimate underlines the need for spatio-temporally high-resolution data to assess heat risks for each precise location and to timely issue hot spot alerts or cool spot recommendations (Weinberger et al., 2018).

Numerous studies have focused on measuring microclimate using weather stations (Chen et al., 2022; Jin et al., 2018; Shi et al., 2016).

* Corresponding author at: Department of Architecture, National University of Singapore, Singapore.
E-mail addresses: kunihiko@nus.edu.sg (K. Fujiwara), maxk@dtu.dk (M. Khomiakov), winstonyym@u.nus.edu (W. Yap), m.ignatius@nus.edu.sg (M. Ignatius), filip@nus.edu.sg (F. Biljecki).

https://doi.org/10.1016/j.scs.2024.105733
Received 8 April 2024; Received in revised form 2 July 2024; Accepted 7 August 2024
Available online 13 August 2024

Public meteorological services globally operate networks of weather stations for regional climate monitoring. It is not possible for these regional weather stations to capture microclimate heterogeneity. Therefore, some buildings or sites deploy their own sensors to monitor their spot microclimate. The collected data are often used to optimize air-conditioning systems (Peng et al., 2022; Yan et al., 2022), to monitor climate-related risks in outdoor spaces (Iwashita & Kobayashi, 2019), to issue hot spot alerts or cool spot recommendations (Yi et al., 2016), and to manage energy consumption by a smart grid (Pashchenko & Rassadin, 2022). However, deploying a dense network of microclimate sensors at an urban scale is impractical due to the high costs and maintenance requirements involved (Liu, Cheng et al., 2022; Maclean et al., 2021).

On the other hand, there has been an increasing number of studies on the physical simulation of microclimate, which traces thermal and fluid dynamics and solves them using a numerical approach and computation (Bachir et al., 2021; Matsuda et al., 2018; Peng et al., 2015). Although these methods offer high-resolution microclimate data in space and time, aligned with the simulation's mesh size and time step, they are constrained by the intricate processes involved in setting boundary conditions, creating 3D models, and collecting thermal property data such as heat capacity, reflectance, transmittance, and evaporation coefficient. Additionally, the physical simulation is computationally demanding if it uses high-resolution meshes and time steps. Furthermore, the results can vary acutely depending on these simulation settings, which can affect robustness and hinders their practical application.

To achieve spatio-temporally high-resolution monitoring for microclimate without dense weather stations, complex setup works, and heavy computational loads, recent studies are exploring the use of machine learning or deep learning techniques for predicting microclimate parameters from urban morphological indicators such as building density and fractional vegetation cover (Alonso & Renard, 2020; Mukonza & Chiang, 2022; Wang et al., 2023). However, open data for these indicators are not readily available; therefore, data collection and calculation for them require time and effort in many cases. Therefore, considerable research has focused on extracting these urban morphological features from street-level, satellite, or aerial imagery using computer vision techniques (Biljecki et al., 2023; Hu et al., 2020; Liu, Li et al., 2022; Xu, Zhang et al., 2023). Street-level imagery, an emerging source of urban information, is gaining popularity due to the availability of data from commercial and crowdsourced data providers (Alvarez Leon & Quinn, 2019; Hou & Biljecki, 2022; Li et al., 2015; Pang & Biljecki, 2022), as well as the ease of collecting one's own data (Ao et al., 2019; He et al., 2020; Kim & Lee, 2022; Wang, Antos et al., 2021). Concurrently, satellite imagery have been readily available for the majority of cities worldwide by some data providers such as Google Earth, and Mapbox. Despite the potential for extracting urban morphological features and the scalability of data sources, a microclimate prediction model that uses street-level, satellite, or aerial imagery and computer vision techniques is yet to be developed.

In this paper, we propose a deep learning model to predict microclimate using street-level and satellite imagery. To realize spatio-temporally high-resolution mapping, the model needs to predict the time-series microclimate, with temporal variation, of a specific location based on imagery data captured at that location. However, it is challenging for a model with solely local imagery inputs to trace temporal variation in a location's microclimate due to mesoscale meteorological phenomena, such as increases in wind speed due to sea-land breezes and decreases in solar radiation due to cloud cover.

Therefore, we define the task of the model as predicting microclimate data at a target location based on microclimate data at a reference location and imagery inputs (Fig. 1). The inputs include microclimate data at a reference location, street-level and satellite imagery from both the target and reference locations. If both locations are within a microscale area, there are no significant variances in climate due to mesoscale meteorological conditions, but there are variances due to heterogeneity in urban morphological features. Thus, by using the reference microclimate data as an input, the model can ignore mesoscale variance and focus on predicting the microclimate difference between the two locations due to urban morphological features (Heusinkveld et al., 2014; Oke, 1982).

We collect microclimate and imagery data in a study area, train and validate the prediction model using the collected dataset. We then create high-resolution microclimate maps using the trained model, and demonstrate the application of these maps for heat health management. This paper aims to address three questions: 'Can imagery data be utilized to predict microclimate?', 'How accurately can microclimate be predicted using imagery data?', and 'How can we utilize the high-resolution microclimate maps in the application for heat health management?'

2. Background and related work

2.1. Impact of urban morphological feature on microclimate

In the domain of meteorology, microclimate is defined as the climatic phenomenon occurring within the microscale, which is smaller than two kilometers horizontally, where the morphological features near the ground surface primarily drive climatic heterogeneity (Orlanski, 1975; Steyn et al., 1981). Concurrently, the mesoscale is defined as the scale from 2 to 2000 km, where meteorological phenomena such as cumulus and cumulonimbus clouds, sea-land breezes, and mountain-valley winds occur (Emanuel, 1986; Orlanski, 1975).

The four key microclimate parameters (air temperature, humidity, wind speed, and radiation) are significantly influenced by urban morphological features, including buildings, vegetation, and ground surfaces. Previous studies have validated their effects through measurements and physical simulations (Chatzidimitriou & Yannas, 2015; Cilek et al., 2024; Haeri et al., 2023; Mughal et al., 2021; Xu et al., 2020).

Dense buildings provide shade for people at street level, thereby reducing solar radiation and air temperature (Bourbia & Boucheriba, 2010; Huang et al., 2008; Middel et al., 2014; Park et al., 2021; Sharmin et al., 2017). Additionally, dense buildings act as wind shields, resulting in observed reductions in wind speed at street level (Kubota et al., 2008; Ng et al., 2011; Peng et al., 2018). However, it is important to note that several studies have reported exceptional cases where high-rise buildings amplify street-level wind speed due to downwash flow, which is wind directed from above to street level along the surfaces of high-rise buildings (Lin et al., 2023; Murakami et al., 1979). Furthermore, building surface materials influence reflectance for solar radiation and heat capacity of building surfaces, affecting solar radiation and air temperature at street level (Tabatabaei & Fayaz, 2023; Yuan et al., 2021). Anthropogenic heat generated by outdoor air-conditioning units and vehicles can also contribute to elevated air temperatures (Chàfer et al., 2022; Kim & Brown, 2021; Xu et al., 2024; Yamamoto et al., 2024; Zhou et al., 2022).

Vegetation, particularly trees, provides shade and reduces solar radiation at street level (Berry et al., 2013; Bode et al., 2014; Heisler, 1986; Konarska et al., 2014; Kuuluvainen & Pukkala, 1989), leading to lower air temperatures (Cai et al., 2022; Huang et al., 2008; Middel et al., 2015; Rahman et al., 2018). Trees and other plants increase humidity through latent heat exchange due to transpiration (Asawa & Fujiwara, 2020; Chen, 1984; Chen et al., 2022; Cheung et al., 2021; Priya & Senthil, 2021; Shiflett et al., 2017; Zhang et al., 2013). Additionally, vegetation acts as a wind shield, reducing wind speed (Park et al., 2012; Ricci et al., 2022; Yuan et al., 2017). Meanwhile, studies have highlighted the impact of vegetation's detailed features, such as leaf density (Oshio & Asawa, 2023), shape of tree crowns (De Abreu-Harbich et al., 2015; Zhang et al., 2020), and arrangements of trees (Fujiwara et al., 2020, 2022; Kim et al., 2023), on microclimate.

Fig. 1. Prediction of microclimate using street-level and satellite imagery.

Ground surfaces significantly influence microclimate. Previous surfaces, like soil and water-retentive pavements, reduce surface and air temperature through water retention and resulting evaporation (Coutts et al., 2013; Elqattan & Elrayies, 2021; Lei et al., 2024; Liu, Ma et al., 2022). Water bodies, such as rivers, lakes, and the sea, also contribute to air temperature reduction and humidity increase through evaporation from their surfaces (Hong et al., 2023; Wong et al., 2012). Conversely, impervious surfaces, such as concrete and asphalt, with higher heat capacities and lacking evaporation, lead to increased surface and air temperatures (Coutts et al., 2013; Elqattan & Elrayies, 2021; Huang et al., 2008). Reflectance of ground surface materials influences solar radiation absorption by the ground, consequently affecting surface and air temperature (Krayenhoff & Voogt, 2010).

2.2. Detection of urban morphological feature using computer vision

The past decade has seen remarkable advancements in deep learning, leading to increased research focused on detecting various urban morphological features from street-level, satellite, and aerial imagery. Furthermore, the emergence of data providers for street-level imagery, such as Google Street View and Baidu Maps, alongside providers for satellite and aerial imagery, like Google Earth and Mapbox, has significantly promoted this research field (Biljecki & Ito, 2021; Kim et al., 2021). It is important to note that this study focuses exclusively on RGB images, which are the most widely spread and used, and does not address multi-spectral imagery.

Street-level imagery offers detailed, pedestrian-perspective information that directly impacts the street-level environment. Therefore, it has been used to evaluate the sky view factor (Biljecki et al., 2023; Liang et al., 2020; Xia et al., 2021; Zeng et al., 2018) and green view index (Ki & Lee, 2021; Liang et al., 2023; Zhang & Zeng, 2024). Furthermore, street-level imagery contain vertical profiles of urban spaces, such as the height of buildings and trees, and building vertical surfaces. For instance, they have been used to estimate the height of buildings (Xu, Zhang et al., 2023; Yan & Huang, 2022), evaluate the H/W aspect ratio of street canyons (Hu et al., 2020), detect individual street trees (Liu, Li et al., 2022; Seiferling et al., 2017), assess the shapes and sizes of street trees (Choi et al., 2022; Liu et al., 2023; Wang et al., 2018), and classify surface materials of buildings (Hosseini et al., 2022; Raghu et al., 2023; Xu, Wong et al., 2023). However, its spatial coverage is limited to streets and roads, omitting areas without street access, such as building rooftops, park interiors, and open spaces around buildings.

Satellite and aerial imagery, conversely, provides a horizontal and homogeneous projection for a certain target area, covering ground surfaces regardless of the presence of streets and roads. Therefore, they have been used to classify land cover types that influence microclimate (Guzder-Williams et al., 2023; Qiu et al., 2019), to detect rooftop greenery (Wu & Biljecki, 2021), to identify building footprints (Chaudhuri et al., 2016; Hamaguchi & Hikosaka, 2018), and to detect tree crowns (Beloiu et al., 2023; Ellis & Mathews, 2019; Timilsina et al., 2020). Additionally, they have been used to calculate two-dimensional indicators for certain areas, such as fractional vegetation cover (Duhl et al., 2012; Furusawa et al., 2023; Kiyono et al., 2022). Although increasing studies estimate information for the vertical direction, such as the height of buildings and trees, there are some limitations in accuracy (Amirkolaee & Arefi, 2019).

The literature review so far indicates that each type of imagery offers distinct advantages. It also suggests that a combination of feature information from both types of imagery enables microclimate prediction models to consider more comprehensive and detailed morphological features, consequently contributing to better performance.

2.3. Related work

Our literature review showed that several studies have presented methods to predict microclimate using statistical methods, machine learning, or deep learning techniques (Alonso & Renard, 2020; Fei et al., 2024; Fu et al., 2022; Gao et al., 2023; Han et al., 2024). However, no study has proposed methods to predict microclimate using street-level, satellite or aerial imagery as inputs for the models. Instead, these studies have used morphological indicators, such as building density, sky view factor, or fractional vegetation cover, as inputs for their prediction models. While this approach helps reduce the number of input dimensions and mitigate model complexity, it may also lead to a lack of significant information, such as the arrangement of buildings or trees, the height of buildings and trees, and the materials for buildings and ground surfaces. Additionally, no study has developed models using statistical approaches, such as machine learning and deep learning, to evaluate all the four primary microclimate parameters: air temperature, humidity, wind speed, and radiation. Thus, there is room to improve the comprehensiveness of microclimate prediction.

Meanwhile, several previous studies suggest potential solutions for the challenges mentioned above, although they do not focus on microclimate prediction. For example, Zhao et al. (2023) developed a

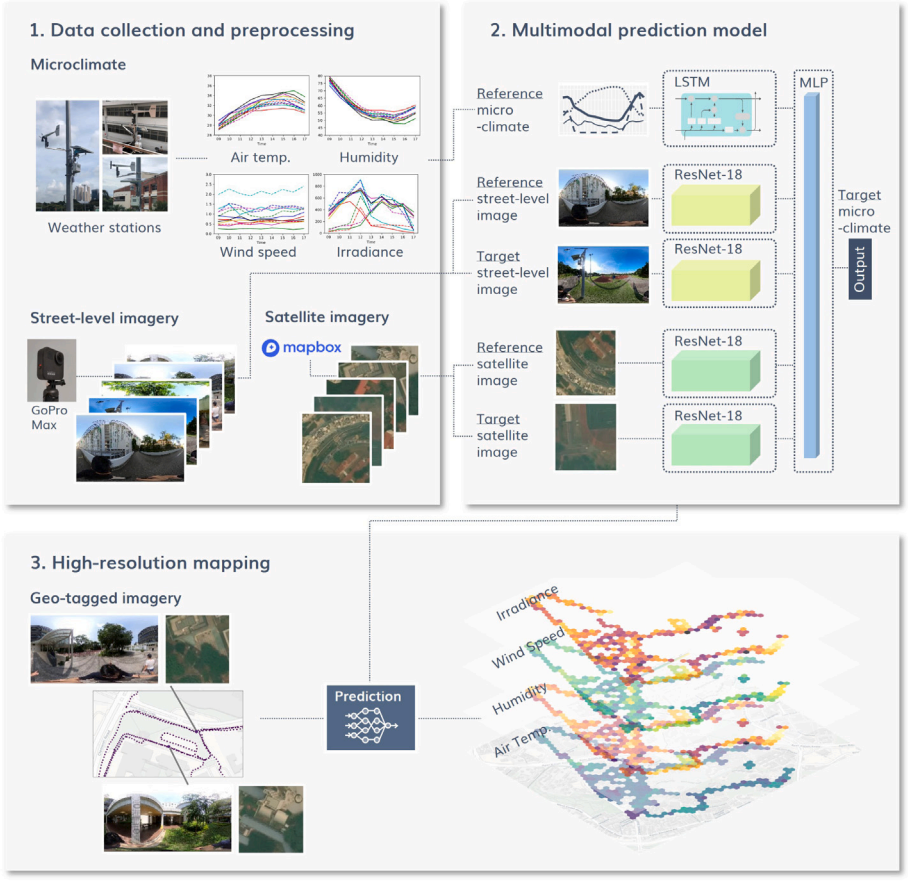

Fig. 2. Overview of our workflow to predict microclimate using street-level and satellite imagery.

CNN-based (Convolutional Neural Network) model to predict the urban acoustic environment from street-level imagery. Their model directly takes a street-level image as its input, enabling consideration of detailed surrounding morphological features to predict noise levels. Huang et al. (2023) proposed a multimodal deep learning model that combined CNN and LSTM (Long Short-Term Memory), to recognize urban villages from street-level and satellite imagery. The multimodal inputs combining two image types enabled the model to consider more comprehensive morphological features than inputs with a single image type. Additionally, Zhang et al. (2021) predicted future microclimate from its past history using LSTM, which can deal with time-series data. The use of LSTM contributed to higher accuracy in predicting microclimate, which is significantly influenced by its past history.

Therefore, we introduce several novelties that have not been the focus of research yet, along with substantial advancements in statistical microclimate prediction. First, we introduce multimodal inputs combining street-level and satellite imagery to predict microclimate, considering more comprehensive morphological features. Second, we predict all four principal parameters: air temperature, humidity, wind speed, and radiation. Third, we develop a multimodal model combining CNN and LSTM, enabling the prediction of microclimate by processing imagery inputs directly and considering the past history of microclimate.

3. Methodology

Our research follows a framework with three main steps, as shown in Fig. 2: (1) Data collection and preprocessing, (2) Multimodal prediction model, and (3) High-resolution mapping. We detail each step in the following subsections.

3.1. Data collection and preprocessing

3.1.1. Microclimate

We focus on four principal microclimate parameters: air temperature (T_{air}), relative humidity (RH), wind speed (v), and global horizontal irradiance (GHI). These parameters are measured by weather stations placed at multiple locations in a study area that is detailed later in Section 4.1. The equipment used in these weather stations is described in Table 1 and Fig. 3. The data, originally recorded at one-minute intervals, is averaged over each hour, following the approaches used in previous studies (Gaudio et al., 2017; Lai et al., 2019). Additionally, we specifically use data collected during the daytime, between 9:00 and 17:00, on clear and rain-free days. To identify clear and rain-free days, we extracted data from days that meet all these conditions: the day's maximum $GHI \geq 900$ W/m^2, the day's minimum $GHI \geq 300$ W/m^2, the day's average $GHI \geq 500$ W/m^2, and the day's accumulated rainfall $= 0$. These preprocessing steps are intended to simplify the task of the prediction model, reduce data size and computational cost, and focus on daytime during clear days, which experience relatively severe heat conditions.

3.1.2. Street-level and satellite imagery

For street-level imagery, there are mainly two types used in research: panoramic and perspective imagery (Biljecki et al., 2023). A panoramic image captures views in all directions, including east, west, north, south and up and down, in one picture using equirectangular projection. In contrast, a perspective image captures a view defined by a specific angle of view, which is captured by a general camera. A perspective view has the advantage that the view is similar to the subjective visible sense of humans; therefore, it is used for studies on urban visual perception (Kruse et al., 2021; Meng et al., 2020;

Table 1
Measured parameters, intervals, sensors, range and accuracy.

Parameter	Interval	Sensor	Range/Accuracy
Air temperature & Relative humidity	1 min	Temperature & humidity sensor (Onset, S-THB-M00x) with solar radiation shield	T_{air}: −40 °C to 70 °C, ±0.2 °C; RH: 0 to 100%, ±2.5%
Wind speed	1 min	Wind speed & Wind direction sensors (RM Young, Wind Monitor AQ Model 05305)	v: 0 to 50 m/s, ±0.2 m/s
Global horizontal irradiance	1 min	Silicon pyranometer (Onset, S-LIB-M003)	0 to 1280 W/m^2, ±10 W/m^2
Rainfall	1 min	Rainfall sensor (ONSET, S-RGB-M002)	0 to 12.7 cm/h, ±1%

Fig. 3. Equipment for weather stations.

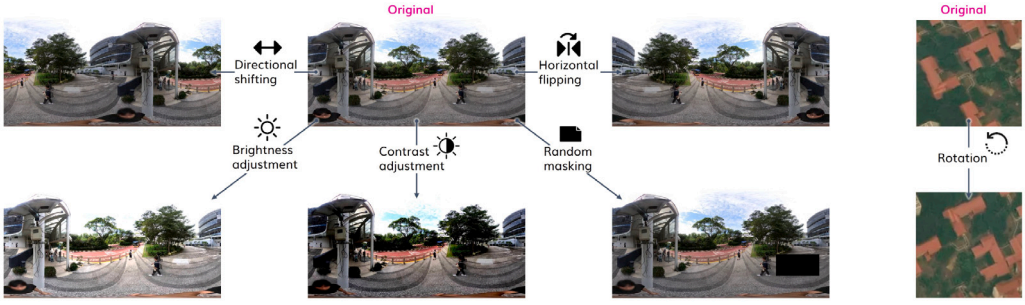

Fig. 4. Data augmentation for street-level and satellite imagery.

Wang et al., 2019; Zhou et al., 2019). However, a perspective view can overlook some significant features due to the constraint in the angle of view. Therefore, to capture urban morphological features of a location more comprehensively, a panoramic image is suitable because of its coverage for all directions, and thus we focus on it in this study.

We use the GoPro Max camera to capture street-level panoramic imagery, processing them with equirectangular projection in the GoPro Player software (version 2.1.29.0). To keep these images at level, we employ the software's 'Horizon Leveling' feature. Around each weather station, we capture 100 images within a 1-meter radius based on the assumption that microclimate variations are negligible within this 1-meter distance. This assumption is supported by many studies that have employed mesh sizes larger than 1 meter for physical simulation of microclimate (Bouketta & Bouchahm, 2020; Cardinali et al., 2020; He et al., 2017; Zhao et al., 2022).

To enhance the generalization performance of our prediction, we use several data augmentation techniques for street-level imagery: horizontal flipping, directional shifting, brightness adjustment, contrast adjustment, and random masking, as illustrated in Fig. 4 (Mikołajczyk & Grochowski, 2018; Shijie et al., 2017; Zhong et al., 2020). For each image, we first apply a 'directional shifting' randomly, varying the angle from 0 to 360 degrees. Then, a 'horizontal flipping' is executed with a 50% probability. After that, we apply either 'brightness adjustment', 'contrast adjustment', or make 'no change' with respective probabilities of 30%, 30%, and 40%. Finally, a 'random masking' is used with a 50% probability.

We gather satellite imagery using the Mapbox Static Tiles API. Mapbox provides a comprehensive global raster tileset with high-resolution satellite and aerial imagery sourced from multiple providers such as NASA, USGS, Maxar, and Nearmaps (as detailed in their documentation: https://docs.mapbox.com/help/glossary/mapbox-satellite/). We acquire satellite imagery at zoom level 19, offering a spatial resolution of 0.149 meters per pixel, and each image covering a 100-meter width in both north-south and east–west directions. We set this 100-meter range based on previous studies (Jusuf et al., 2014; Yu et al., 2020). Jusuf et al. (2014) and Yu et al. (2020) indicate that the averaged morphological features within a 50-meter radius can adequately explain the microclimate parameters observed at the central point of the circle. Around each weather station, we downloaded 100 satellite images, randomly changing the center points of the satellite images within a 20-meter radius area. We apply the same data augmentation techniques as those used with the street-level imagery, with one key difference: instead of directional shifting, we use rotation for the satellite imagery, as illustrated on the right side in Fig. 4.

3.2. Multi-modal prediction model

We propose a multimodal prediction model that combines LSTM, ResNet-18, and MLP (Multilayer Perceptron) architectures (Fig. 5). This model uses microclimate data from a reference location and both street-level and satellite images from the reference and target locations as inputs. Accordingly, the model has five input branches: an LSTM branch for reference microclimate data, ResNet-18 branches for target and reference street-level images, and ResNet-18 branches for reference and target satellite images. Its output is the predicted value for a microclimate parameter, one of T_{air}, RH, v, and GHI, at a target timestamp at the target location.

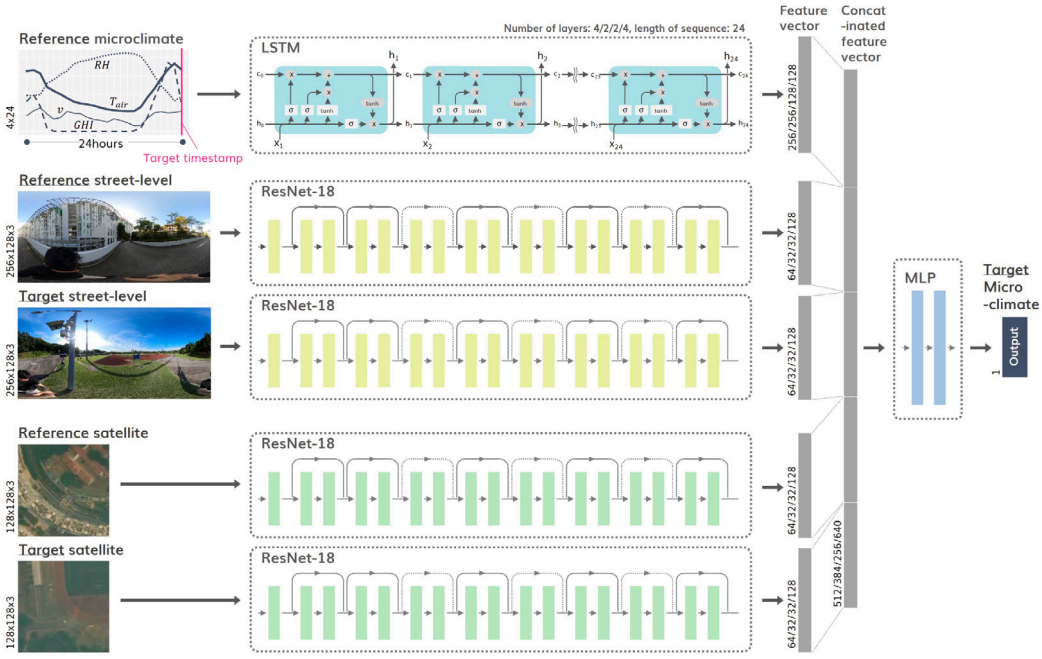

Fig. 5. Architecture of multi-modal prediction model. Numbers next to the input images show the width/height in pixels. The numbers above the LSTM branch shows the numbers of layers in the models for $T_{air}/RH/v/GHI$, while numbers next to the feature vectors indicate the numbers of dimensions in the models for $T_{air}/RH/v/GHI$.

The input microclimate data is time-series hourly data for a 24-hour period, which includes the target timestamp and the 23 preceding timestamps, and consists of four parameters: T_{air}, RH, v, and GHI. Input microclimate parameters for each timestamp, denoted as X_t, are fed separately into each LSTM block. The first LSTM block processes X_1 and outputs the cell state vector C_1 and the hidden state vector h_1. The subsequent LSTM block receives C_1, h_1, and X_2, processes them, and outputs C_2 and h_2. This sequential processing continues across 24 LSTM blocks. Ultimately, only the final hidden state vector h_{24} from the last block is used in the subsequent processing step.

Unlike the input microclimate data, the street-level and satellite images are not time-series. Each Resnet-18 branch processes an image input and outputs a feature vector by aggregating spatial patterns through a convolutional neural network with residual connections (He et al., 2015). The model is intended to identify static urban morphological features in the images that affect microclimate, regardless of time. While significant seasonal changes, like leaf fall or snow cover, can influence microclimate, we choose a study area with minimal seasonal variation. Therefore, we do not factor in seasonal changes. The model's output is solely one microclimate parameter at the target timestamp; therefore, we train separate models for each parameter. This approach ensures that each model has its own optimal weights to capture features in imagery inputs that significantly influence each microclimate parameter. For each model corresponding to one parameter, we set a different number of layers for LSTM branch and vary the number of dimension for the feature vectors from each branch to improve performance.

3.3. High-resolution mapping

To create spatio-temporally high-resolution microclimate maps of an area, we collect time-series microclimate data at a reference location within the area using a weather station. We then capture corresponding street-level and satellite images at the location. Additionally, we gather dense geo-tagged street-level and satellite imagery within the area. For street-level imagery, we use a GoPro Max camera equipped with an internal GPS for geo-tagging. Satellite imagery is downloaded from the same locations as the street-level imagery using the Mapbox Static Tiles API. We input these data into our model to predict microclimate data at each location where a geo-tagged image is captured and for each timestamp when reference microclimate data is collected. We then construct meshes with a 50-meter width and calculate a representative microclimate value for each cell by averaging the values of locations within it.

4. Experiment

We conducted an experiment in a study area to validate our model, and to demonstrate its practical applications through high-resolution mapping of microclimate. The following subsections detail each part in the experiment.

4.1. Study area

The study was conducted at the National University of Singapore's campus, situated around 8 km from downtown Singapore (Fig. 6). Singapore is situated in a tropical climate zone (Beck et al., 2018), and does not experience significant seasonal variation in urban morphological features, such as falling leaves and snow coverage. The campus, surrounded primarily by residential areas, covers an area of about 150 hectares. It extends around 2 km in the north-south direction and 1.7 km east–west, which falls within the microscale range defined as smaller than 2 km (Orlanski, 1975; Steyn et al., 1981). Thus, we can attribute differences in climate conditions within this study area primarily to heterogeneity in morphological features.

4.2. Dataset for training and validation

4.2.1. Microclimate

We collected microclimate data from 12 weather stations in the study area between February 2019 and April 2020. Details about the weather station equipment are provided in Section 3.1.1. All weather stations were installed at a height of 3 to 5 meters above the ground. We extracted data at daytime from 9:00 to 17:00 on clear and rain-free days from the collected original data. The extracted data with similar weather conditions showed a similar diurnal variation trend. Fig. 7 presents examples of the extracted microclimate data. The most

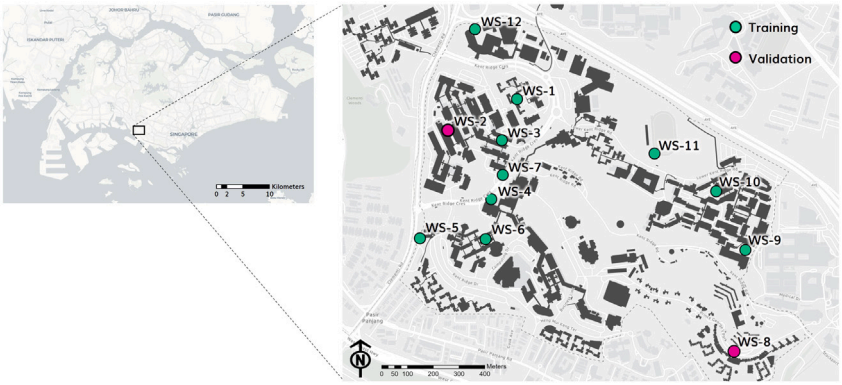

Fig. 6. Study area and locations of weather stations. Basemap: (c) OpenStreetMap contributors.

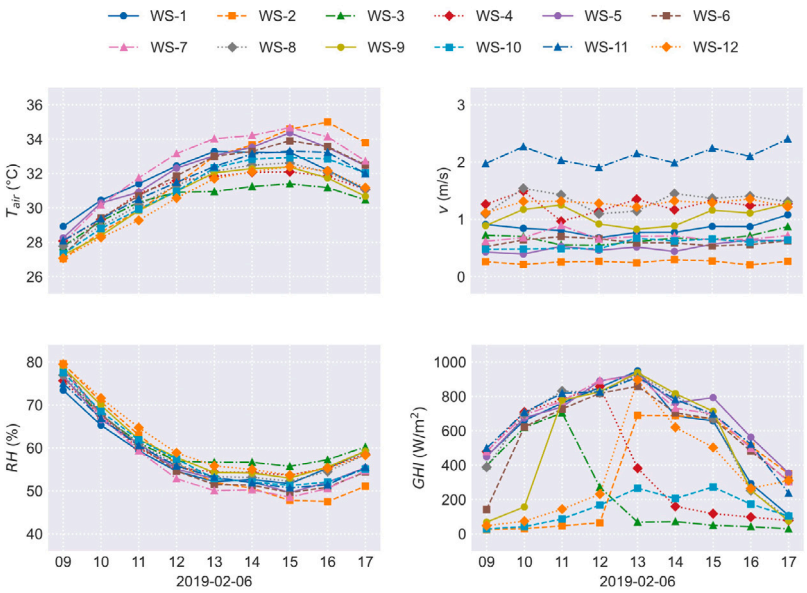

Fig. 7. Examples of the microclimate data measured by the weather stations.

important suggestion from this is that there are significant differences among weather stations, indicating that microclimate prediction contributes to understanding the significant heterogeneity of heat risk in this area. For T_{air}, values change within the range from 27 to 35 °C. The maximum difference among weather stations reaches approximately 4 °C. For RH, values change within the range from 45% to 80%, and the maximum difference reaches around 10%. For v, the values are within the range from 0.2 to 2.3 m/s, and the maximum difference reaches approximately 2.0 m/s. For GHI, the value ranges from 0 to 900 W/m^2, and the maximum difference reaches around 800 W/m^2. We attribute the significant variability of GHI among weather stations to the heterogeneity in the arrangements of surrounding shading objects. As shown in Fig. 8, some weather stations, especially WS-11, feature significant openness with less shading objects, while others, especially WS-10, are surrounded by shading objects such as tree crowns and buildings. Such heterogeneity in surrounding urban morphology could also explain the substantial variance in v.

4.2.2. Street-level and satellite imagery

In May 2023, we acquired street-level imagery, and in December 2023, we collected satellite imagery using Mapbox Static Tiles API. There was a time gap for about four years between microclimate data collection in 2019 and this imagery data collection in 2023. Therefore, we compared the photos taken around the weather stations in 2019, with the collected street-level and satellite imagery in 2023. Through this comparison, we confirmed that there was no significant change in the surrounding morphological features in the time gap. We collected 100 street-level images and 100 satellite images for each weather station, resulting in a total of 1200 street-level images and 1200 satellite images. Fig. 8 presents examples of the collected street-level and satellite imagery. The data augmentation techniques described in Section 3.1.2 were applied to each street-level and satellite image.

4.3. Dataset for high-resolution mapping

To create a high-resolution map, we required reference microclimate data and imagery, as well as dense geo-tagged images as target imagery. For the reference microclimate data and imagery, we used the dataset described in Sections 4.2.1 and 4.2.2. As the target imagery, we captured geo-tagged street-level and satellite imagery along pedestrian paths in the study area. We captured street-level imagery at 4612 locations along the main walking paths in the study area using the GoPro Max camera (Fig. 9). We then downloaded the corresponding satellite imagery from the same locations as the street-level imagery using the Mapbox Static Tiles API. Apart from code we developed and released openly as open-source software, our geo-tagged street-level imagery is released openly on Mapillary (https://www.mapillary.com/app/user/kunihiko/), ensuring the reproducibility of the work. We capture panoramic imagery ourselves due to the insufficient coverage

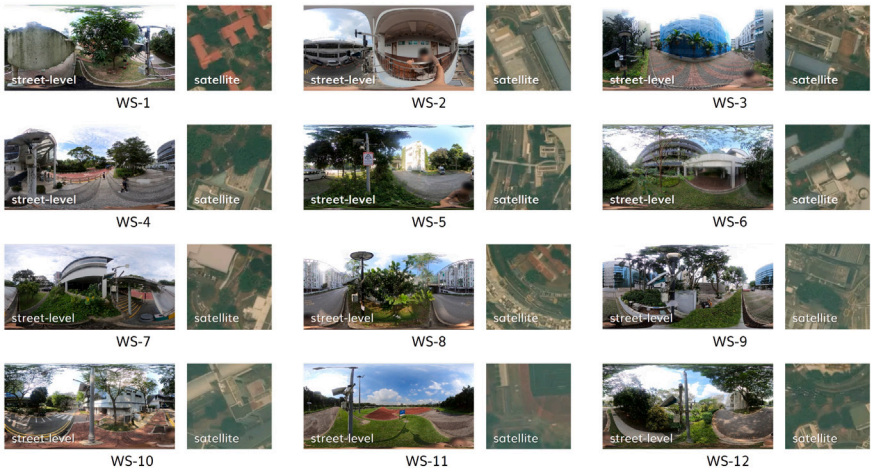

Fig. 8. Examples of the collected street-level and satellite imagery.

Fig. 9. Map of locations for capturing geo-tagged street-level imagery. Basemap: (c) OpenStreetMap contributors.

by commercial and crowdsourced data providers in our study area. However, panoramic imagery from such data providers can also be used for our method if the target area has sufficient data available.

4.4. Experiment setup for validation

The purpose of the validation in the experiment is to evaluate spatial generalization performance of our model. For the task of the model, this spatial generalization performance refers to the model's ability to predict unknown microclimate data at a target location not included in the training dataset. This ability is crucial for creating high-resolution maps of microclimate using dense geo-tagged street-level and satellite imagery. To assess this, we divided the twelve weather stations into two groups — training and validation — as depicted in Fig. 6, and created two corresponding datasets. For the validation group, we selected two weather stations that exhibited significant difference in microclimate and location. As presented in Table 2, both the training and validation datasets used the data collected by the training weather stations as reference microclimate data. The target microclimate for the training dataset comprised data collected exclusively by the training weather stations. Conversely, the target microclimate for the validation dataset included data exclusively collected by the validation weather stations.

For the experiment, we integrated the collected microclimate data with street-level and satellite imagery to create the dataset. Fig. 10 illustrates an example data point from the dataset. To compose one data point, we first randomly assigned a reference and a target weather station following the selection for the training and validation datasets shown in Table 2. For the training dataset, both the reference and target weather stations were selected from WS-1, 3, 4, 5, 6, 7, 9, 10, 11, and 12. For the validation dataset, the reference weather station was selected from the same group, whereas the target weather station was selected from WS-2 and 8. Each weather station had 100 street-level and 100 satellite images. Therefore, we employed one street-level image and one satellite image as reference, and employed one street-level image and one satellite image as target from them. We then randomly determined a target timestamp and set the reference microclimate data with four parameters — T_{air}, RH, v, and GHI — as hourly time-series data for 24 h. Finally, we set the target microclimate data at the target timestamp. We trained the model individually for each microclimate parameter using separately created datasets; therefore, the target microclimate data for each dataset contained only one of four parameters. By repeating these processes for a data point, we created a training dataset with 10,000 data points, and a validation dataset with 5000 data points for each parameter.

Table 2
Breakdown of weather stations by training and validation datasets, and by reference and target. For example, the number '1' represents 'WS-1'.

	Reference	Target
Training	1, 3, 4, 5, 6, 7, 9, 10, 11, 12	1, 3, 4, 5, 6, 7, 9, 10, 11, 12
Validation	1, 3, 4, 5, 6, 7, 9, 10, 11, 12	2, 8

We employ RMSE (Root Mean Square Error), MAE (Mean Absolute Error) and R^2 (coefficient of determination) as the indicators for the

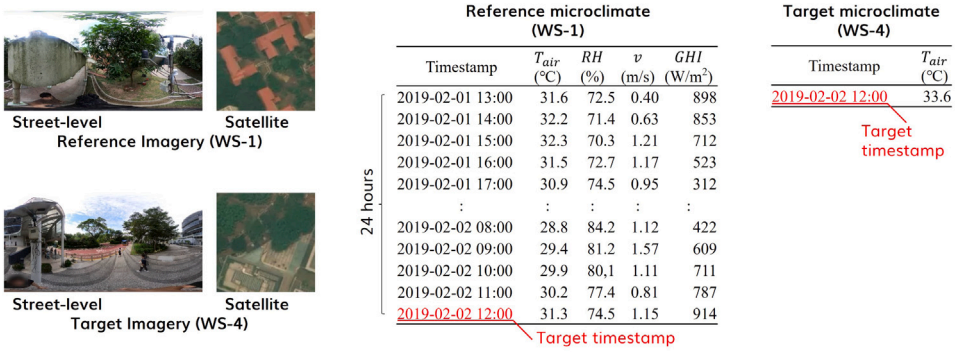

Fig. 10. Example data point from the dataset.

performance. They are calculated using Eqs. (1), (2), and (3), respectively. Note that R^2 is not actually squared; therefore it can have a negative value when the data exhibits a negative correlation trend.

$$RMSE(y,\hat{y}) = \sqrt{\frac{1}{n}\sum_{i=1}^{n}(y_i - \hat{y}_i)^2} \tag{1}$$

$$MAE(y,\hat{y}) = \frac{1}{n}\sum_{i=1}^{n}|y_i - \hat{y}_i| \tag{2}$$

$$R^2(y,\hat{y}) = 1 - \frac{\sum_{i=1}^{n}(y_i - \hat{y}_i)^2}{\sum_{i=1}^{n}(y_i - \bar{y})^2} \tag{3}$$

where $\hat{y}_i$ is the predicted value of the i-th sample and y_i is the corresponding true value for total n samples, and $\bar{y} = \frac{1}{n}\sum_{i=1}^{n} y_i$.

5. Results and analysis

5.1. Performance

Fig. 11 displays the performance across each model for every microclimate parameter. The baseline in Fig. 11 was a model that simply reproduced the input reference microclimate parameters; that is, the error metrics for the baseline were calculated by directly comparing the reference and target microclimate parameters. To evaluate the impact of different input types on performance, we devised four scenarios. In Scenario-1, we used only the LSTM branch for reference microclimate inputs, while disabling the ResNet-18 branches for imagery inputs. Scenario-2 involved the use of the ResNet-18 branches for street-level imagery and the LSTM branch. In Scenario-3, we employed the ResNet-18 branches for satellite imagery alongside the LSTM branch. Scenario-4 integrated all the branches with all the input types.

The comparison between the baseline and the four scenarios shows that the performances of every scenario are superior to the baseline across all the combinations of error metrics and microclimate parameter. This indicates that the model has predictive ability. Furthermore, the performances of scenarios that use imagery inputs — Scenario-2, Scenario-3, and Scenario-4 — are superior to that of Scenario-1 across all combinations. This suggests that street-level and satellite imagery inputs contribute to improving the accuracy.

For all error metrics and microclimate parameters, except for MAE for T_{air}, RH, and GHI, Scenario-4 performs the best. It is followed by either Scenario-2 or Scenario-3. This suggests that the combination of street-level and satellite imagery inputs, offering more comprehensive urban morphological information, helps Scenario-4 outperform Scenario-2 and Scenario-3 that use inputs with a single imagery type. The RMSE, MAE values of Scenario-4 are 0.95 °C and 0.69 °C for T_{air}, 2.57% and 1.97% for RH, and 0.31 m/s and 0.27 m/s for v. The differences in T_{air}, RH, and v of around 1.0 °C, 3.0%, and 0.3 m/s, respectively, do not significantly impact heat risk and thermal comfort; therefore, the performance is sufficient for these practical applications.

The RMSE and MAE values of Scenario-4 for GHI are 225 W/m^2 and 189 W/m^2, respectively. Although the values are not sufficiently low, the model still achieves some accuracy, as these values are lower compared to the baseline. The R^2 values of Scenario-4 for T_{air}, v, and GHI are 0.82, 0.94, and 0.67, respectively, indicating sufficient accuracy. The R^2 value of 0.39 for GHI, while indicating some accuracy, is relatively low.

The lower R^2 of GHI could be explained by the fact that solar radiation is a strongly localized microclimate phenomenon in contrast with T_{air}, RH, and v. Even small differences in the positions of shading objects, such as tree crowns and buildings, can significantly impact GHI values. For example, in a location surrounded by trees, whether the location receives direct solar radiation at a given time significantly depends on the specific height and direction of the tree crowns. This locality could reduce the robustness of the correlation between GHI values and surrounding morphological features, and thus, could make it difficult for the model to predict GHI. Furthermore, v is a more localized parameter compared to T_{air} and RH, though not as localized as GHI. Its spatial variability depends on the proximity or positional relationship to wind-shielding objects, and on wind direction. This accounts for the lower R^2 for v compared to T_{air} and RH. Additionally, although the Scenario-4 outperformed the other scenarios, the performances of Scenario-2, Scenario-3, and Scenario-4 for T_{air} and RH are not substantially different. This suggests that the difference in the explanatory power for T_{air} and RH among the three image input types — panoramic, satellite, and the combination of these two — are not substantial. Meanwhile, for v and GHI, the performances of Scenario-2 and Scenario-4 show significantly higher accuracy compared to Scenario-3, suggesting that the input types including street-level imagery have substantially stronger explanatory power for v and GHI than that solely including satellite imagery. This could also be explained by the locality of v and GHI; that is, the more local morphological information from street-level imagery contributes to higher accuracy compared to the more global morphological information from satellite imagery.

Fig. 12 illustrates hexbin density plots with ground truths on the x-axis and prediction results on the y-axis. This shows that the predicted values for T_{air}, RH, and v exhibit normal noise and align closely with the target values, whereas the predicted values for GHI show less alignment. This corresponds to the results of R^2 presented in Fig. 11. The plots for T_{air}, v, and GHI show trends that the model overestimates in the lower ranges, below 34 °C, 1.0 m/s, and 200 W/m^2, respectively, while it underestimates in the higher ranges above these thresholds. The plot for RH has a similar trend, although the overestimation or underestimation is insignificant. We attribute these trends to biases between the training and validation datasets. For example, WS-2, which was included only in the validation dataset, records the highest T_{air} among all weather stations at 16:00 and 17:00 (Fig. 7). Predicting such extreme values can be challenging for a model trained on a dataset that excludes data from such extreme conditions.

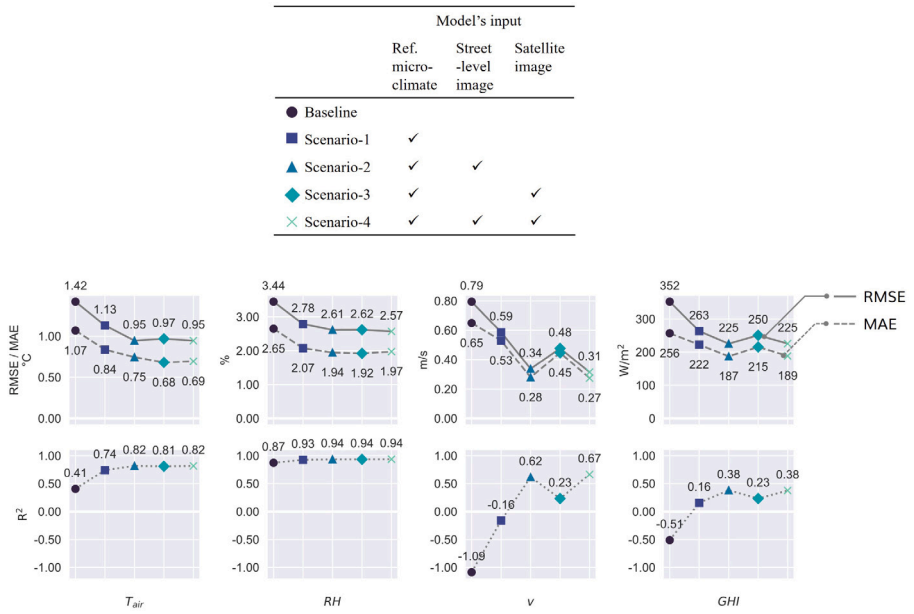

Fig. 11. Comparison of model performance. The table above details the combinations of input types for each scenario and their corresponding legends. In the line chart below, solid, dashed, and dotted lines represent RMSE, MAE, and R^2, respectively.

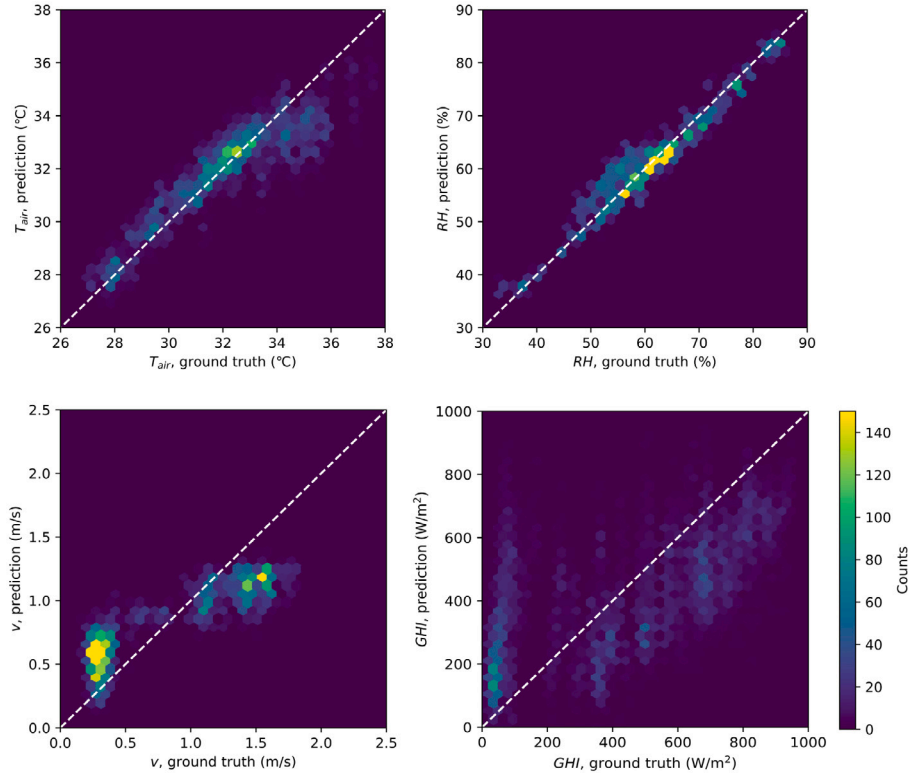

Fig. 12. Hexbin density plots illustrating the correlation between model predictions and ground truth. White dashed lines represent the x = y line.

Fig. 13 illustrates examples of prediction results, showing diurnal time-series comparisons between the reference (WS-4), the predictions, and the ground truths for target-1 (WS-2) and target-2 (WS-8). We predicted each value for the target microclimate using data from WS-4 as the reference microclimate input for the model. Note that both target-1 and target-2 were included in the validation weather stations; therefore, the ground truth data of the model's output for these two locations were not included in the training dataset. The predictions align closely with the ground truths, although there are some gaps between the predictions and the ground truths under certain conditions, such as for target-1 from 14:00 to 17:00 for T_{air}, RH, and GHI. This corresponds to the trend of underestimation or overestimation indicated in Fig. 12.

Based on the results so far, we conclude that the model with all the input types (Scenario-4) provides sufficient spatial generalization performance for T_{air}, RH and v for practical applications. Additionally, although the performance for GHI is relatively low compared to the other parameters, it remains valuable for certain purposes, such as

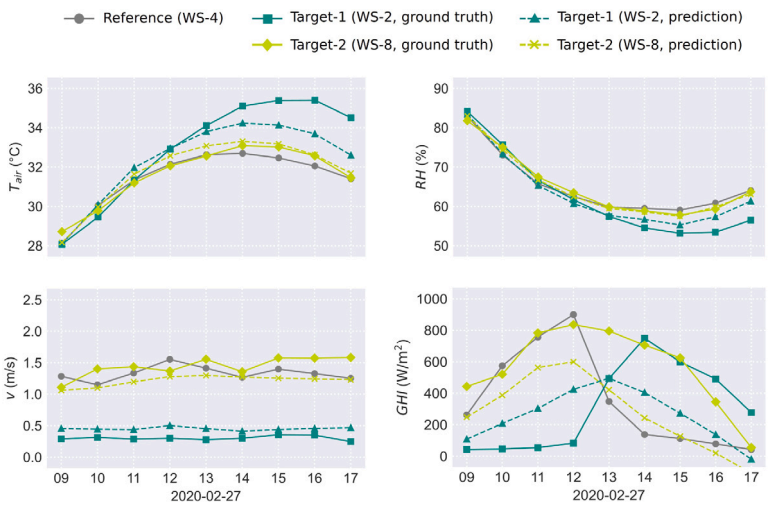

Fig. 13. Time-Series plot demonstrating model predictions alongside ground truth in a day.

capturing rough trends in spatial distribution. In our environment, equipped with a NVIDIA GeForce RTX 4090 Ti GPU with 24 GB memory, the processing time of the model with all the input types for one data point was 4.9 ms, indicating a speed that is quick enough for practical applications.

5.2. High-resolution mapping

We created high-resolution microclimate maps of the study area using the collected geo-tagged imagery and the trained model (Fig. 14). The date and time of the maps were set to February 1, 2019, at 14:00, with data from WS-6 as the reference microclimate. We employed a hexagon grid with a width of approximately 50 m.

As shown in Fig. 14, for T_{air}, a location with higher value is characterized by low buildings, impervious ground surfaces, and a lack of vegetation. This corresponds to the findings from previous studies that showed anthropogenic heat from buildings, the higher heat capacity of impervious ground surfaces, and a lack of cooling effect from evapotranspiration contribute to the elevated T_{air} (Berry et al., 2013; Chàfer et al., 2022; Coutts et al., 2013; Elqattan & Elrayies, 2021; Huang et al., 2008; Kim & Brown, 2021). For RH, a location with higher value features a significant presence of vegetation, corresponding to the findings of previous studies that reported the higher RH caused by transpiration (Cheung et al., 2021; Zhang et al., 2013). For v and GHI, locations with higher values show their significant openness. This corresponds to the findings from previous studies that indicated lower v and GHI resulted from the shading and wind-shielding effect of dense buildings and vegetation (Bode et al., 2014; Kubota et al., 2008; Kuuluvainen & Pukkala, 1989; Ng et al., 2011; Peng et al., 2018).

Fig. 15 illustrates an example of high-resolution maps for T_{air} with hourly time-series from 9:00 to 14:00 on February 1 in 2019. The spatial distribution characteristics of T_{air} vary with time; therefore, each map for each timestamp has its unique hot spots and cool spots. These maps are expected to serve various purposes. For instance, they could be used for issuing hot spot alerts, recommending cool spots, and identifying optimal walking routes based on the predicted high-resolution microclimate. This could mitigate the risks associated with extreme urban heat for pedestrians or outdoor workers (Sun et al., 2024; Wang, Ren et al., 2024). Urban planners could also utilize these maps to incorporate shading elements in areas vulnerable to heat (Buo et al., 2023; Nyelele & Kroll, 2021), or to preserve heat-sensitive plant and animal species in cooler areas (Kemppinen et al., 2024; Percival, 2023). Additionally, the maps could facilitate detailed calculations of building energy consumption and the optimization of HVAC (heating, ventilation, and air conditioning) systems and lighting operations, based on microclimate (Dougherty & Jain, 2023; Wang, Liu et al., 2021; Xu et al., 2022). This approach could contribute to the decarbonization of buildings. Considering the quick processing time of the model, it could be extended to support urban digital twins with real-time and high-resolution microclimate mapping. The assumed use cases suggest the potential of our method to build sustainable cities with enhanced heat resilience, biodiversity, and energy efficiency.

6. Discussion

6.1. Impact of selections of weather station for training and validation datasets

In Section 5.1, we confirmed some spatial generalization performance of the model using datasets with a specific selection of training and validation weather stations, as described in Fig. 6 and Table 2. However, this selection could have influenced the model's performance, suggesting that different selections might yield different performances. Therefore, we assessed and compared the performances of models trained on datasets with different selections of weather stations (Fig. 16). Fig. 16 illustrates this comparison with the RMSE performed by Baseline, Scenario-1, and Scenario-2 for each microclimate parameter. The definitions for Scenario-1 and 2 are the same as those in Fig. 11. Both Scenario-1 and Scenario-2 consistently outperformed the Baseline across all datasets and all microclimate parameters, indicating that these models possess spatial generalization performance that is robust to the selection of weather stations. Moreover, Scenario-2 generally outperforms Scenario-1 in most datasets and microclimate parameters, suggesting that imagery inputs enhance performance, regardless of the selection of weather stations. However, certain datasets indicate relatively lower accuracy. For example, RMSE for v by both Scenario-1 and Scenario-2 under the datasets 'Excl. WS-11' are higher than those under the other datasets. More specifically, although the RMSE for Scenario-1 and Scenario-2 are lower than the Baseline, the margins of improvement over the Baseline are narrower compared to the other datasets. An example of street-level imagery in Fig. 8 reveals that WS-11 is characterized by its exceptional openness relative to other locations. Corresponding to this openness, WS-11 recorded the highest v among all weather stations (Fig. 7). Predicting such extreme conditions with a model trained on a dataset excluding the data from WS-11 could pose significant challenges. We attribute the observed lower accuracy to this bias between training and validation datasets.

Based on the results, we conclude that although the selection of weather stations can cause bias between training and validation datasets and influence the resulting performance, the model is capable

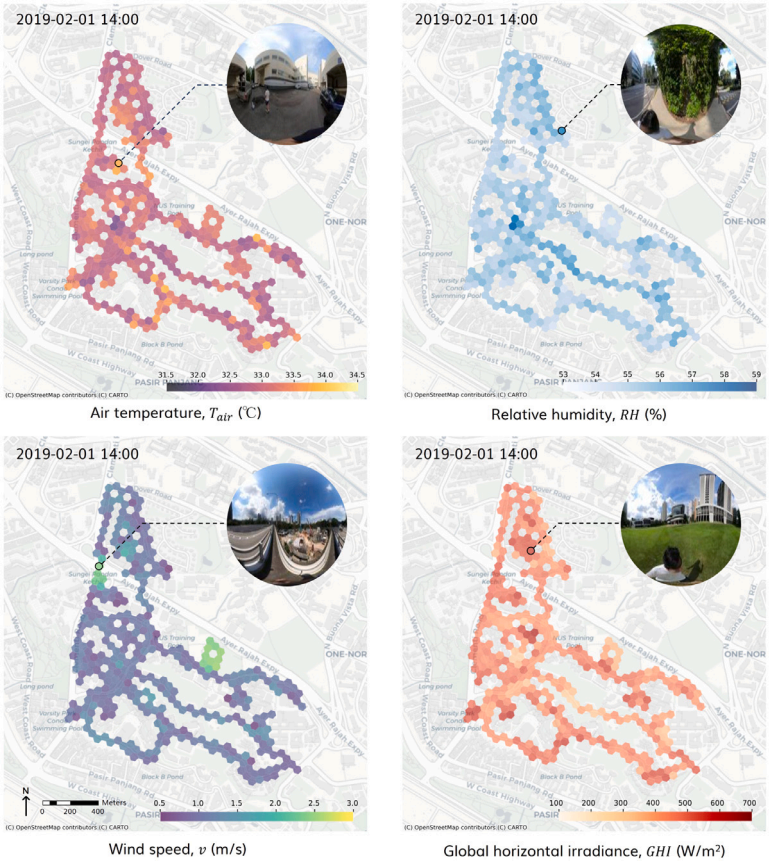

Fig. 14. High-resolution maps depicting predicted microclimate variations. Basemap: (c) OpenStreetMap contributors.

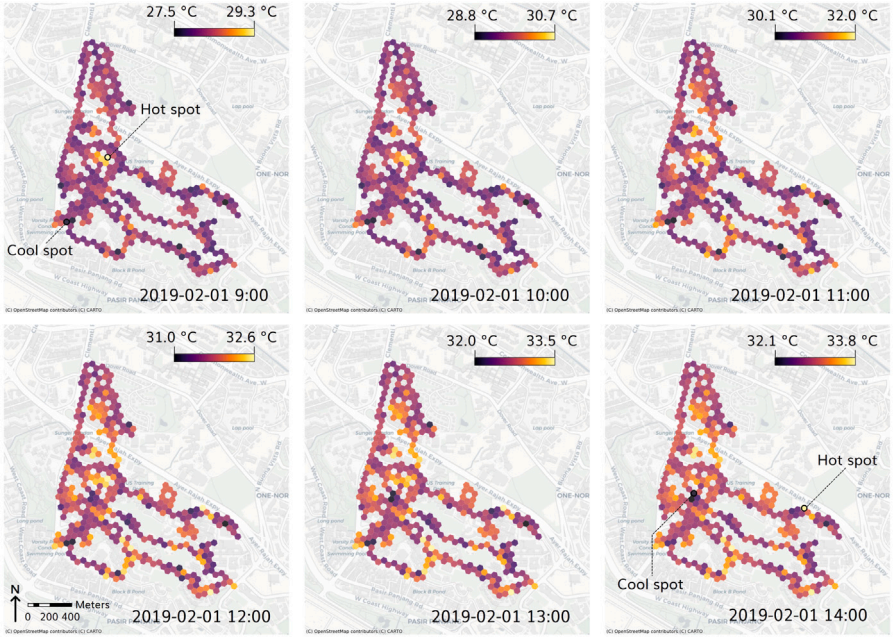

Fig. 15. High-resolution map depicting predicted T_{air} variations with diurnal time-series. Basemap: (c) OpenStreetMap contributors.

of achieving a certain level of performance independently of this selection. To mitigate the bias and improve the robustness of the model's performance, increasing the number of locations by adding weather stations or by traverse measurements with mobile weather stations would be effective.

6.2. Limitation and direction for future work

The results so far demonstrated some spatial generalization performance of our proposed model; however, this performance is confined to the study area. Consequently, models trained on our dataset are

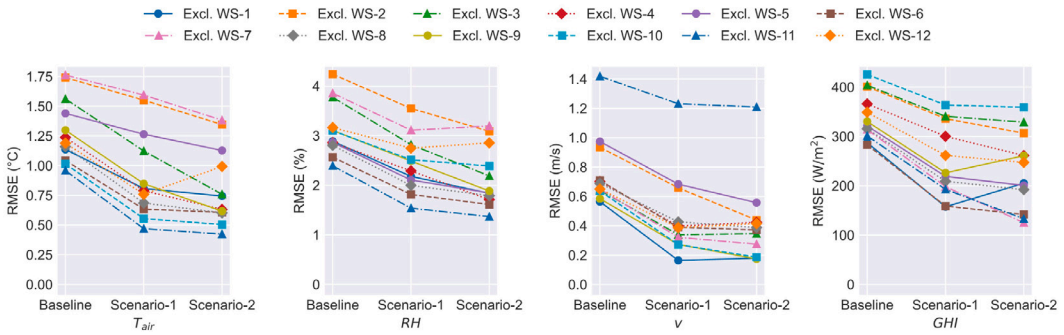

Fig. 16. Comparison of model performance across datasets with varying selections of training and validation groups for weather stations. Each line corresponds to a dataset defined by a specific selection. For example, the notation "excl. WS-1" in the legend indicates that the training group excludes WS-1, while the validation group includes it exclusively.

not suitable for application in other areas. To achieve a more comprehensive spatial generalization performance that is applicable across a variety of areas, it is essential to develop a more comprehensive dataset. The datasets used in this study were derived from data collected within a university campus in Singapore, situated in a tropical climate zone. To encompass a broader range of environmental conditions, the dataset should include data from different climate zones, such as dry, temperate, and continental climates (Beck et al., 2018). Additionally, our study area lacks features like dense high-rise constructions or significant water bodies; therefore, our model is currently unable to account for variations such as increased wind speed by high-rise buildings (Lin et al., 2023; Murakami et al., 1979) or decreased air temperature due to the cooling effects of evaporation from water surfaces (Hong et al., 2023; Wong et al., 2012). The dataset should encompass data from areas with distinct morphological and thermal properties compared to our study area. Despite regional difference, similar trends have been observed globally in the association between microclimate and urban morphology, such as the reduction in air temperature due to dense vegetation (Cai et al., 2022; Middel et al., 2015; Rahman et al., 2018) and decreased wind speed by dense buildings (Liu et al., 2020; Peng et al., 2018; Wang et al., 2020). This suggests that with more comprehensive datasets that include diverse urban morphological features, our model could potentially be generalized to various cities worldwide.

Additionally, there are some important factors that this study does not address. For example, information regarding the direction in the street-level panoramic imagery in our datasets was disabled because we randomly changed the direction of panoramic imagery to prioritize data augmentation. If we add wind direction, sun position, direct and diffuse solar irradiance to the input microclimate data, and properly adjust the direction of panoramic imagery, the performances for v and GHI could be improved. As mentioned in Section 5.1, solar radiation might be too local a phenomenon for statistical approaches like ours to predict accurately. Another approach that judges the existence of shading objects by plotting the sun position on a segmented panoramic image would be more effective (Deng, Yang et al., 2021; Gong et al., 2019). It would be effective to choose a proper approach for each microclimate parameter. Furthermore, we did not address seasonal change by selecting a study area with insignificant seasonal variations. If we apply our model to another area with significant seasonal variation, we must consider this. To address this, for example, training an exclusive model by preparing a separate dataset for each season would be effective.

Furthermore, there is room for investigation regarding the projection type of the input street-level imagery. Our method employs panoramic imagery to capture street-level and detailed morphological features. However, to enhance the scalability of this method, it would be preferable to use perspective imagery which is readily available in numerous cities through crowdsourced data providers. The model could potentially achieve sufficient performance with the perspective input, considering that Biljecki et al. (2023) confirmed the usability of perspective images in evaluating urban morphological metrics, such as the sky view factor and green view index. We need to validate performances by comparing the results from panoramic imagery with those from perspective imagery.

Our method does not require dense networks of weather stations during inference phase for predicting microclimate parameters using a trained model. This is because our approach is not based on interpolation, but rather on predicting the microclimate of one target location from that of one reference location using imagery inputs. It only needs one weather station to be installed per microscale area to create a high-resolution microclimate map of the area. Considering that a weather station can cover a circle with a radius of two kilometers — the horizontal distance defining a microscale — our method can be applied to city-scale microclimate mapping, provided that we address the comprehensiveness of the dataset and the resulting city-scale generalization performance of the model.

7. Conclusions

To address the increasing demand for heat health management without relying on dense weather stations and heavy computational loads, we proposed a multimodal deep learning model which combines LSTM and ResNet-18 architectures to predict microclimate using street-level and satellite imagery, which have not been used for this purpose previously. Taking a study area situated at a university campus in Singapore, we collected microclimate data using weather stations, and captured street-level and satellite imagery. We trained and validated our prediction model using collected datasets. Furthermore, we created high-resolution microclimate maps using the trained model and geotagged imagery data in the study area, and demonstrated its practical application. This research resulted in the following key contributions and findings.

1. We confirmed the model's predictive ability; thus, this paper proposes a cost efficient method to capture high-resolution microclimate dynamics compared to measurement with weather stations and physical simulation.
2. We observed a contribution of street-level and satellite imagery inputs to prediction accuracy by comparing models with and without these imagery inputs. This presents a new utilization of street-level and satellite imagery.
3. We demonstrated practical applications of high-resolution microclimate maps, such as identifying hot spots and cool spots for each time of a day. This use case is expected to be utilized for issuing heat alerts and cool spot recommendations, and suggesting optimal walking routes to avoid heat risks.

In recent years, the concept of urban digital twin has gained increasing attention as a tool for managing and operating cities by utilizing real-time information that is digitally mirrored with the actual cities (Deng, Zhang et al., 2021; Ignatius et al., 2024; Jiang et al., 2022; Lehtola et al., 2022; Lei et al., 2023). Our findings underscore the importance of urban digital twins with high-resolution and real-time microclimate mapping to address the challenges posed by heat risks and improve the health and well-being of urban dwellers. Such a microclimate digital twin offers a valuable tool for urban planners, policymakers, and the public to make informed decisions about sustainable urban planning, green infrastructure design, and emergency response strategies.

CRediT authorship contribution statement

Kunihiko Fujiwara: Conceptualization, Methodology, Software, Validation, Formal analysis, Investigation, Data Curation, Writing – original draft, Writing – review & editing. **Maxim Khomiakov:** Methodology, Software, Writing – review & editing. **Winston Yap:** Methodology, Software, Writing – review & editing. **Marcel Ignatius:** Methodology, Investigation, Data Curation, Writing – review & editing. **Filip Biljecki:** Conceptualization, Methodology, Supervision, Project administration, Funding acquisition, Writing – review & editing.

Declaration of competing interest

The authors declare that they have no known competing financial interests or personal relationships that could have appeared to influence the work reported in this paper.

Data availability

Data will be made available on request.

Declaration of Generative AI and AI-assisted technologies in the writing process

During the preparation of this work the authors used ChatGPT in order to proofread the text. After using this tool, the authors reviewed and edited the content as needed and take full responsibility for the content of the publication.

Acknowledgments

We gratefully acknowledge the comments by the editor and reviewers. We express our gratitude to the members of the NUS Urban Analytics Lab for the valuable discussions. Special thanks go to Yu Dayu and Liang Xiucheng for their insightful advice on coding the prediction models and writing. This research has been supported by Takenaka Corporation and is part of the projects (i) Large-scale 3D Geospatial Data for Urban Analytics, which is supported by the National University of Singapore under the Start Up Grant; (ii) Multi-scale Digital Twins for the Urban Environment: From Heartbeats to Cities, which is supported by the Singapore Ministry of Education Academic Research Fund Tier 1; (iii) NUS Resilience and Growth Postdoctoral Fellowship – Smart Cities and Urban Analytics, which is funded by the National Research Foundation (NRF), Singapore; (iv) Development of a Multiscale Urban Microclimate Model for NUS Campus Thermal Environment (funded by NUS). We would like to thank the Singapore International Graduate Award (SINGA) scholarship provided by the Agency for Science, Technology, and Research (A*STAR) and the NUS.

References

Alonso, L., & Renard, F. (2020). A new approach for understanding urban microclimate by integrating complementary predictors at different scales in regression and machine learning models. *Remote Sensing*, *12*(15), 2434.

Alvarez Leon, L. F., & Quinn, S. (2019). The value of crowdsourced street-level imagery: examining the shifting property regimes of OpenStreetCam and Mapillary. *GeoJournal*, *84*(2), 395–414.

Amirkolaee, H. A., & Arefi, H. (2019). Height estimation from single aerial images using a deep convolutional encoder-decoder network. *ISPRS Journal of Photogrammetry and Remote Sensing*, *149*, 50–66.

Ao, Y., Wang, J., Zhou, M., Lindenbergh, R. C., & Yang, M. Y. (2019). Fully convolutional networks for street furniture identification in panorama images. *XLII-2-W13*, In *ISPRS geospatial week 2019 (volume XLII-2/w13) - 10–14 June 2019, Enschede, The Netherlands* (pp. 13–20). Copernicus GmbH.

Arellana, J., Saltarín, M., Larrañaga, A. M., González, V. I., & Henao, C. A. (2020). Developing an urban bikeability index for different types of cyclists as a tool to prioritise bicycle infrastructure investments. *Transportation Research Part A: Policy and Practice*, *139*, 310–334.

Asawa, T., & Fujiwara, K. (2020). Estimation of sensible and latent heat fluxes of an isolated tree in Japanese summer. *Boundary-Layer Meteorology*, *175*(3), 417–440.

Azegami, Y., Imanishi, M., Fujiwara, K., & Kusaka, H. (2023). Effects of solar radiation in the streets on pedestrian route choice in a city during the summer season. *Building and Environment*, *235*, Article 110250.

Bachir, N., Bounoua, L., Aiche, M., Maliki, M., Nigro, J., & El Ghazouani, L. (2021). The simulation of the impact of the spatial distribution of vegetation on the urban microclimate: A case study in Mostaganem. *Urban Climate*, *39*, Article 100976.

Beck, H. E., Zimmermann, N. E., McVicar, T. R., Vergopolan, N., Berg, A., & Wood, E. F. (2018). Present and future Köppen-Geiger climate classification maps at 1-km resolution. *Sci Data*, *5*, Article 180214.

Beloiu, M., Heinzmann, L., Rehush, N., Gessler, A., & Griess, V. C. (2023). Individual Tree-Crown detection and species identification in heterogeneous forests using aerial RGB imagery and deep learning. *Remote Sensing*, *15*(5), 1463.

Berry, R., Livesley, S. J., & Aye, L. (2013). Tree canopy shade impacts on solar irradiance received by building walls and their surface temperature. *Building and Environment*, *69*, 91–100.

Biljecki, F., & Ito, K. (2021). Street view imagery in urban analytics and GIS: A review. *Landscape and Urban Planning*, *215*, Article 104217.

Biljecki, F., Zhao, T., Liang, X., & Hou, Y. (2023). Sensitivity of measuring the urban form and greenery using street-level imagery: A comparative study of approaches and visual perspectives. *International Journal of Applied Earth Observation and Geoinformation*, *122*, Article 103385.

Bode, C. A., Limm, M. P., Power, M. E., & Finlay, J. C. (2014). Subcanopy solar radiation model: Predicting solar radiation across a heavily vegetated landscape using LiDAR and GIS solar radiation models. *Remote Sensing of Environment*, *154*, 387–397.

Bouketta, S., & Bouchahm, Y. (2020). Numerical evaluation of urban geometry's control of wind movements in outdoor spaces during winter period. Case of mediterranean climate. *Renewable Energy*, *146*, 1062–1069.

Bourbia, F., & Boucheriba, F. (2010). Impact of street design on urban microclimate for semi arid climate (Constantine). *Renewable Energy*, *35*(2), 343–347.

Buo, I., Sagris, V., Jaagus, J., & Middel, A. (2023). High-resolution thermal exposure and shade maps for cool corridor planning. *Sustainable Cities and Society*, *93*, Article 104499.

Cai, Y., Li, C., Ye, L., Xiao, L., Gao, X., Mo, L., Du, H., Zhou, Y., & Zhou, G. (2022). Effect of the roadside tree canopy structure and the surrounding on the daytime urban air temperature in summer. *Agricultural and Forest Meteorology*, *316*, Article 108850.

Cardinali, M., Pisello, A. L., Piselli, C., Pigliautile, I., & Cotana, F. (2020). Microclimate mitigation for enhancing energy and environmental performance of Near Zero Energy Settlements in Italy. *Sustainable Cities and Society*, *53*, Article 101964.

Chàfer, M., Tan, C. L., Cureau, R. J., Hien, W. N., Pisello, A. L., & Cabeza, L. F. (2022). Mobile measurements of microclimatic variables through the central area of Singapore: An analysis from the pedestrian perspective. *Sustainable Cities and Society*, *83*, Article 103986.

Chatzidimitriou, A., & Yannas, S. (2015). Microclimate development in open urban spaces: The influence of form and materials. *Energy and Buildings*, *108*, 156–174.

Chaudhuri, D., Kushwaha, N. K., Samal, A., & Agarwal, R. C. (2016). Automatic building detection from high-resolution satellite images based on morphology and internal gray variance. *IEEE Journal of Selected Topics in Applied Earth Observations and Remote Sensing*, *9*(5), 1767–1779.

Chen, J. (1984). Uncoupled multi-layer model for the transfer of sensible and latent heat flux densities from vegetation. *Boundary-Layer Meteorology*, *28*(3), 213–225.

Chen, S., Wong, N. H., Ignatius, M., Zhang, W., He, Y., Yu, Z., & Hii, D. J. C. (2022). ATLAS: Software for analysing the relationship between urban microclimate and urban morphology in a tropical city. *Building and Environment*, *208*, Article 108591.

Cheung, P. K., Jim, C. Y., & Siu, C. T. (2021). Effects of urban park design features on summer air temperature and humidity in compact-city milieu. *Applied Geography*, *129*, Article 102439.

Choi, K., Lim, W., Chang, B., Jeong, J., Kim, I., Park, C.-R., & Ko, D. W. (2022). An automatic approach for tree species detection and profile estimation of urban street trees using deep learning and Google street view images. *ISPRS Journal of Photogrammetry and Remote Sensing*, *190*, 165–180.

Cilek, A., Unal, M., & Middel, A. (2024). The effects of 2-D and 3-D urban landscape metrics on mean radiant temperature in hot-arid Phoenix and Tempe, Arizona, USA. *Sustainable Cities and Society*, *101*, Article 105116.

Coutts, A. M., Tapper, N. J., Beringer, J., Loughnan, M., & Demuzere, M. (2013). Watering our cities: The capacity for water sensitive urban design to support urban cooling and improve human thermal comfort in the Australian context. *Progress in Physical Geography: Earth and Environment*, *37*(1), 2–28.

De Abreu-Harbich, L. V., Labaki, L. C., & Matzarakis, A. (2015). Effect of tree planting design and tree species on human thermal comfort in the tropics. *Landscape and Urban Planning*, *138*, 99–109.

Deng, M., Yang, W., Chen, C., Wu, Z., Liu, Y., & Xiang, C. (2021). Street-level solar radiation mapping and patterns profiling using Baidu Street View images. *Sustainable Cities and Society*, *75*, Article 103289.

Deng, T., Zhang, K., & Shen, Z.-J. m. (2021). A systematic review of a digital twin city: A new pattern of urban governance toward smart cities. *Journal of Management Science and Engineering*, *6*(2), 125–134.

Dougherty, T. R., & Jain, R. K. (2023). Invisible walls: Exploration of microclimate effects on building energy consumption in New York City. *Sustainable Cities and Society*, *90*, Article 104364.

Duhl, T. R., Guenther, A., & Helmig, D. (2012). Estimating urban vegetation cover fraction using Google Earth® images. *Journal of Land Use Science*, *7*(3), 311–329.

Ellis, E. A., & Mathews, A. J. (2019). Object-based delineation of urban tree canopy: assessing change in Oklahoma City, 2006–2013. *Computers, Environment and Urban Systems*, *73*, 85–94.

Elqattan, A. A., & Elrayies, G. M. (2021). Developing a novel solar-driven cool pavement to improve the urban microclimate. *Sustainable Cities and Society*, *64*, Article 102554.

Emanuel, K. A. (1986). Overview and definition of mesoscale meteorology. In P. S. Ray (Ed.), *Mesoscale meteorology and forecasting* (pp. 1–17). Boston, MA: American Meteorological Society.

Fei, F., Xiao, Y., Wang, L., Wang, Y., Fukuda, H., Yao, W., Yu, H., & Dong, Q. (2024). A novel approach for quantifying the influence intensity of urban water and greenery resources on microclimate for efficient utilization. *Sustainable Cities and Society*, Article 105597.

Fu, J., Wang, Y., Zhou, D., & Cao, S.-J. (2022). Impact of urban park design on microclimate in cold regions using newly developped prediction method. *Sustainable Cities and Society*, *80*, Article 103781.

Fujiwara, K., Asawa, T., & Kiyono, T. (2020). Optimization and evaluation of tree arrangement in open space for urban heat adaptation and heat island mitigation. *Journal of Environmental Engineering*, *85*(772), 475–484.

Fujiwara, K., Asawa, T., & Kiyono, T. (2022). Multi-objective optimization for tree arrangement in urban open space considering thermal radiant environment and scenery. *AIJ Journal of Technology and Design*, *28*(68), 320–325.

Furusawa, T., Koera, T., Siburian, R., Wicaksono, A., Matsudaira, K., & Ishioka, Y. (2023). Time-series analysis of satellite imagery for detecting vegetation cover changes in Indonesia. *Scientific Reports*, *13*(1), 8437.

Gao, Y., Zhao, J., & Han, L. (2023). Quantifying the nonlinear relationship between block morphology and the surrounding thermal environment using random forest method. *Sustainable Cities and Society*, *91*, Article 104443.

Gaspari, J., & Fabbri, K. (2017). A study on the use of outdoor microclimate map to address design solutions for urban regeneration. *Energy Procedia*, *111*, 500–509.

Gaudio, N., Gendre, X., Saudreau, M., Seigner, V., & Balandier, P. (2017). Impact of tree canopy on thermal and radiative microclimates in a mixed temperate forest: A new statistical method to analyse hourly temporal dynamics. *Agricultural and Forest Meteorology*, *237–238*, 71–79.

Gong, F.-Y., Zeng, Z.-C., Ng, E., & Norford, L. K. (2019). Spatiotemporal patterns of street-level solar radiation estimated using Google Street View in a high-density urban environment. *Building and Environment*, *148*, 547–566.

Guzder-Williams, B., Mackres, E., Angel, S., Blei, A. M., & Lamson-Hall, P. (2023). Intra-urban land use maps for a global sample of cities from Sentinel-2 satellite imagery and computer vision. *Computers, Environment and Urban Systems*, *100*, Article 101917.

Haeri, T., Hassan, N., & Ghaffarianhoseini, A. (2023). Evaluation of microclimate mitigation strategies in a heterogenous street canyon in Kuala Lumpur from outdoor thermal comfort perspective using Envi-met. *Urban Climate*, *52*, Article 101719.

Hamaguchi, R., & Hikosaka, S. (2018). Building detection from satellite imagery using ensemble of size-specific detectors. In *2018 IEEE/CVF conference on computer vision and pattern recognition workshops* CVPRW, (pp. 223–2234). openaccess.thecvf.com.

Hamdan, D. M. A., & de Oliveira, F. L. (2019). The impact of urban design elements on microclimate in hot arid climatic conditions: Al Ain City, UAE. *Energy and Buildings*, *200*, 86–103.

Han, J., Chong, A., Lim, J., Ramasamy, S., Wong, N. H., & Biljecki, F. (2024). Microclimate spatio-temporal prediction using deep learning and land use data. *Building and Environment*, *253*, Article 111358.

He, H., Lin, X., Yang, Y., & Lu, Y. (2020). Association of street greenery and physical activity in older adults: A novel study using pedestrian-centered photographs. *Urban Forestry and Urban Greening*, *55*, Article 126789.

He, Y., Yu, H., Ozaki, A., Dong, N., & Zheng, S. (2017). A detailed investigation of thermal behavior of green envelope under urban canopy scale in summer: A case study in Shanghai area. *Energy and Buildings*, *148*, 142–154.

He, K., Zhang, X., Ren, S., & Sun, J. (2015). Deep residual learning for image recognition. In *Proc. IEEE comput. soc. conf. comput. vis. pattern recognit.* (pp. 770–778). openaccess.thecvf.com.

Heisler, G. M. (1986). Effects of individual trees on the solar radiation climate of small buildings. *Urban Ecology*, *9*(3), 337–359.

Heusinkveld, B. G., Steeneveld, G. J., van Hove, L. W. A., Jacobs, C. M. J., & Holtslag, A. A. M. (2014). Spatial variability of the Rotterdam urban heat island as influenced by urban land use. *Journal of Geophysical Research: Atmospheres*, *119*(2), 677–692.

Hong, C., Qu, Z., Xu, W., & Gu, Z. (2023). Study on water cooling island effects under different climatic conditions. *City and Built Environment*, *1*(1), 4.

Hosseini, M., Miranda, F., Lin, J., & Silva, C. T. (2022). CitySurfaces: City-scale semantic segmentation of sidewalk materials. *Sustainable Cities and Society*, *79*, Article 103630.

Hou, Y., & Biljecki, F. (2022). A comprehensive framework for evaluating the quality of street view imagery. *International Journal of Applied Earth Observation and Geoinformation*, *115*, Article 103094.

Hu, C.-B., Zhang, F., Gong, F.-Y., Ratti, C., & Li, X. (2020). Classification and mapping of urban canyon geometry using Google Street View images and deep multitask learning. *Building and Environment*, *167*, Article 106424.

Huang, L., Li, J., Zhao, D., & Zhu, J. (2008). A fieldwork study on the diurnal changes of urban microclimate in four types of ground cover and urban heat island of Nanjing, China. *Building and Environment*, *43*(1), 7–17.

Huang, Y., Zhang, F., Gao, Y., Tu, W., Duarte, F., Ratti, C., Guo, D., & Liu, Y. (2023). Comprehensive urban space representation with varying numbers of street-level images. *Computers, Environment and Urban Systems*, *106*, Article 102043.

Ignatius, M., Lim, J., Gottkehaskamp, B., Fujiwara, K., Miller, C., & Biljecki, F. (2024). Digital twin and wearables unveiling pedestrian comfort dynamics and walkability in cities. *X-4-W5-2024*, In *ISPRS TC IV (WG IV/9)
19th 3D geoInfo conference 2024 - 1–3 July 2024, Vigo, Spain* (pp. 195–202). Copernicus GmbH.

Ito, K., & Biljecki, F. (2021). Assessing bikeability with street view imagery and computer vision. *Transportation Research Part C: Emerging Technologies*, *132*, Article 103371.

Iwashita, H., & Kobayashi, F. (2019). Transition of meteorological variables while downburst occurrence by a high density ground surface observation network. *Journal of Wind Engineering and Industrial Aerodynamics*, *184*, 153–161.

Jiang, F., Ma, L., Broyd, T., Chen, W., & Luo, H. (2022). Digital twin enabled sustainable urban road planning. *Sustainable Cities and Society*, *78*, Article 103645.

Jin, H., Cui, P., Wong, N. H., & Ignatius, M. (2018). Assessing the effects of urban morphology parameters on microclimate in Singapore to control the urban heat island effect. *Sustainability: Science, Practice and Policy*, *10*(1), 206.

Jusuf, S. K., Wong, N. H., Wong, Z. Y., & Tan, E. (2014). Transformation of industrial planning in Singapore: Study on the microclimatic condition of different industrial estates. *Building and Environment*, *80*, 48–60.

Kemppinen, J., Lembrechts, J. J., Van Meerbeek, K., Carnicer, J., Chardon, N. I., Kardol, P., Lenoir, J., Liu, D., Maclean, I., Pergl, J., Saccone, P., Senior, R. A., Shen, T., Słowińska, S., Vandvik, V., von Oppen, J., Aalto, J., Ayalew, B., Bates, O., ... De Frenne, P. (2024). Microclimate, an important part of ecology and biogeography. *Global Ecology and Biogeography*, *33*(6).

Ki, D., & Lee, S. (2021). Analyzing the effects of Green View Index of neighborhood streets on walking time using Google Street View and deep learning. *Landscape and Urban Planning*, *205*, Article 103920.

Kim, Y. J., & Brown, R. D. (2021). A multilevel approach for assessing the effects of microclimatic urban design on pedestrian thermal comfort: The high line in New York. *Building and Environment*, *205*, Article 108244.

Kim, S.-N., & Lee, H. (2022). Capturing reality: Validation of omnidirectional video-based immersive virtual reality as a streetscape quality auditing method. *Landscape and Urban Planning*, *218*, Article 104290.

Kim, J. H., Lee, S., Hipp, J. R., & Ki, D. (2021). Decoding urban landscapes: Google street view and measurement sensitivity. *Computers, Environment and Urban Systems*, *88*, Article 101626.

Kim, J. Y., Park, C. Y., Hyun, J. H., Kim, S. H., Yun, S. H., Lee, D. K., & Kim, J. Y. (2023). Landscape design for improved thermal environment: An optimized tree arrangement design for Climate-Responsive outdoor spaces in residential buildings complexes. *Sustainable Cities and Society*, *97*, Article 104762.

Kiyono, T., Fujiwara, K., & Tsurumi, R. (2022). Development and evaluation of an open dataset for vegetation cover fraction in each town block across Japan using Google Earth Engine. *AIJ Journal of Technology and Design*, *28*(68), 521–526.

Konarska, J., Lindberg, F., Larsson, A., Thorsson, S., & Holmer, B. (2014). Transmissivity of solar radiation through crowns of single urban trees—application for outdoor thermal comfort modelling. *Theoretical and Applied Climatology*, *117*(3), 363–376.

Kotharkar, R., & Ghosh, A. (2022). Progress in extreme heat management and warning systems: A systematic review of heat-health action plans (1995–2020). *Sustainable Cities and Society*, *76*, Article 103487.

Kousis, I., Manni, M., & Pisello, A. L. (2022). Environmental mobile monitoring of urban microclimates: A review. *Renewable and Sustainable Energy Reviews*, *169*, Article 112847.

Kousis, I., Pigliautile, I., & Pisello, A. L. (2021). Intra-urban microclimate investigation in urban heat island through a novel mobile monitoring system. *Scientific Reports*, *11*(1), 9732.

Krayenhoff, E. S., & Voogt, J. A. (2010). Impacts of urban albedo increase on local air temperature at Daily–Annual time scales: Model results and synthesis of previous work. *Journal of Applied Meteorology and Climatology*, *49*(8), 1634–1648.

Kruse, J., Kang, Y., Liu, Y.-N., Zhang, F., & Gao, S. (2021). Places for play: Understanding human perception of playability in cities using street view images and deep learning. *Computers, Environment and Urban Systems*, *90*, Article 101693.

Kubota, T., Miura, M., Tominaga, Y., & Mochida, A. (2008). Wind tunnel tests on the relationship between building density and pedestrian-level wind velocity: Development of guidelines for realizing acceptable wind environment in residential neighborhoods. *Building and Environment*, *43*(10), 1699–1708.

Kumar, P., & Sharma, A. (2020). Study on importance, procedure, and scope of outdoor thermal comfort –A review. *Sustainable Cities and Society*, *61*, Article 102297.

Kuuluvainen, T., & Pukkala, T. (1989). Simulation of within-tree and between-tree shading of direct radiation in a forest canopy: effect of crown shape and sun elevation. *Ecological Modelling*, *49*(1), 89–100.

Lai, X., Tang, Y., Li, L., Chan, P., & Zeng, Q. (2019). Study on microclimate observation network for urban unit: A case study in a campus of Shenzhen, China. *Physics and Chemistry of the Earth, Parts A/B/C*, *110*, 117–124.

Lehtola, V. V., Koeva, M., Elberink, S. O., Raposo, P., Virtanen, J.-P., Vahdatikhaki, F., & Borsci, S. (2022). Digital twin of a city: Review of technology serving city needs. *International Journal of Applied Earth Observation and Geoinformation*, *114*, Article 102915.

Lei, Y., He, Y., Li, X., Tian, Y., Xiang, X., & Feng, C. (2024). Experimental comparison on the performance of radiative, reflective and evaporative cooling in extremely hot climate: A case study in Chongqing, China. *Sustainable Cities and Society*, *100*, Article 105023.

Lei, B., Janssen, P., Stoter, J., & Biljecki, F. (2023). Challenges of urban digital twins: A systematic review and a Delphi expert survey. *Automation in Construction*, *147*, Article 104716.

Li, Y., Ouyang, W., Yin, S., Tan, Z., & Ren, C. (2023). Microclimate and its influencing factors in residential public spaces during heat waves: An empirical study in Hong Kong. *Building and Environment*, *236*, Article 110225.

Li, X., Zhang, C., Li, W., Ricard, R., Meng, Q., & Zhang, W. (2015). Assessing street-level urban greenery using Google Street View and a modified Green View Index. *Urban Forestry and Urban Greening*, *14*(3), 675–685.

Liang, J., Gong, J., Zhang, J., Li, Y., Wu, D., & Zhang, G. (2020). GSV2SVF-an interactive GIS tool for sky, tree and building view factor estimation from street view photographs. *Building and Environment*, *168*, Article 106475.

Liang, X., Zhao, T., & Biljecki, F. (2023). Revealing spatio-temporal evolution of urban visual environments with street view imagery. *Landscape and Urban Planning*, *237*, Article 104802.

Lin, Q., Ishida, Y., Tanaka, H., Mochida, A., Yang, Q., & Tamura, Y. (2023). Large eddy simulations of strong wind mechanisms at pedestrian level around square-section buildings with same aspect ratios and different sizes. *Building and Environment*, *243*, Article 110680.

Liu, Z., Cheng, K. Y., He, Y., Jim, C. Y., Brown, R. D., Shi, Y., Lau, K., & Ng, E. (2022). Microclimatic measurements in tropical cities: Systematic review and proposed guidelines. *Building and Environment*, *222*, Article 109411.

Liu, D., Jiang, Y., Wang, R., & Lu, Y. (2023). Establishing a citywide street tree inventory with street view images and computer vision techniques. *Computers, Environment and Urban Systems*, *100*, Article 101924.

Liu, Y., Li, D., Wan, S., Wang, F., Dou, W., Xu, X., Li, S., Ma, R., & Qi, L. (2022). A long short-term memory-based model for greenhouse climate prediction. *International Journal of Intelligent Systems*, *37*(1), 135–151.

Liu, Y., Ma, H., Zhang, C., & Luo, X. (2022). Watering on porous pavement for improvement of environmental human thermal comfort in an ecological community in arid area: A case study in Lanzhou, China. *Sustainable Cities and Society*, *85*, Article 104081.

Liu, Y., Xu, Y., Zhang, F., & Shu, W. (2020). A preliminary study on the influence of Beijing urban spatial morphology on near-surface wind speed. *Urban Climate*, *34*, Article 100703.

Maclean, I. M. D., Duffy, J. P., Haesen, S., Govaert, S., De Frenne, P., Vanneste, T., Lenoir, J., Lembrechts, J. J., Rhodes, M. W., & Van Meerbeek, K. (2021). On the measurement of microclimate. *Methods in Ecology and Evolution*, *12*(8), 1397–1410.

Matsuda, K., Onishi, R., & Takahashi, K. (2018). Tree-crown-resolving large-eddy simulation coupled with three-dimensional radiative transfer model. *Journal of Wind Engineering and Industrial Aerodynamics*, *173*, 53–66.

Meng, Y., Xing, H., Yuan, Y., Wong, M. S., & Fan, K. (2020). Sensing urban poverty: From the perspective of human perception-based greenery and open-space landscapes. *Computers, Environment and Urban Systems*, *84*, Article 101544.

Middel, A., Chhetri, N., & Quay, R. (2015). Urban forestry and cool roofs: Assessment of heat mitigation strategies in Phoenix residential neighborhoods. *Urban Forestry and Urban Greening*, *14*(1), 178–186.

Middel, A., Häb, K., Brazel, A. J., Martin, C. A., & Guhathakurta, S. (2014). Impact of urban form and design on mid-afternoon microclimate in Phoenix local climate zones. *Landscape and Urban Planning*, *122*, 16–28.

Mikołajczyk, A., & Grochowski, M. (2018). Data augmentation for improving deep learning in image classification problem. In *2018 international interdisciplinary phD workshop* iIPhDW, (pp. 117–122). IEEE.

Mughal, M. O., Kubilay, A., Fatichi, S., Meili, N., Carmeliet, J., Edwards, P., & Burlando, P. (2021). Detailed investigation of vegetation effects on microclimate by means of computational fluid dynamics (CFD) in a tropical urban environment. *Urban Climate*, *39*, Article 100939.

Mukonza, S. S., & Chiang, J.-L. (2022). Micro-climate computed machine and deep learning models for prediction of surface water temperature using satellite data in Mundan water reservoir. *Water*, *14*(18), 2935.

Murakami, S., Uehara, K., & Komine, H. (1979). Amplification of wind speed at ground level due to construction of high-rise building in urban area. *Journal of Wind Engineering and Industrial Aerodynamics*, *4*(3), 343–370.

Ng, E., Yuan, C., Chen, L., Ren, C., & Fung, J. C. H. (2011). Improving the wind environment in high-density cities by understanding urban morphology and surface roughness: A study in Hong Kong. *Landscape and Urban Planning*, *101*(1), 59–74.

Nyelele, C., & Kroll, C. N. (2021). A multi-objective decision support framework to prioritize tree planting locations in urban areas. *Landscape and Urban Planning*, *214*, Article 104172.

Oke, T. R. (1982). The energetic basis of the urban heat island. *Quarterly Journal of the Royal Meteorological Society*, *108*(455), 1–24.

Orlanski, I. (1975). A rational subdivision of scales for atmospheric processes. *Bulletin of the American Meteorological Society*, *56*(5), 527–530.

Oshio, H., & Asawa, T. (2023). Simulating the 3D distribution of absorbed shortwave radiation in a tree crown: Comparison of simplified and Monte Carlo models. *Journal of Geophysical Research*, *128*(21).

Pang, H. E., & Biljecki, F. (2022). 3D building reconstruction from single street view images using deep learning. *International Journal of Applied Earth Observation and Geoinformation*, *112*, Article 102859.

Park, Y., Guldmann, J.-M., & Liu, D. (2021). Impacts of tree and building shades on the urban heat island: Combining remote sensing, 3D digital city and spatial regression approaches. *Computers, Environment and Urban Systems*, *88*, Article 101655.

Park, M., Hagishima, A., Tanimoto, J., & Narita, K.-I. (2012). Effect of urban vegetation on outdoor thermal environment: Field measurement at a scale model site. *Building and Environment*, *56*, 38–46.

Pashchenko, A. F., & Rassadin, Y. M. (2022). Microclimate monitoring system design for the smart grid analysis and constructive parameters estimation. *IFAC-PapersOnLine*, *55*(9), 479–484.

Pedersen Zari, M., MacKinnon, M., Varshney, K., & Bakshi, N. (2022). Regenerative living cities and the urban climate–biodiversity–wellbeing nexus. *Nature Climate Change*, *12*(7), 601–604.

Peng, Y., Lei, Y., Tekler, Z. D., Antanuri, N., Lau, S.-K., & Chong, A. (2022). Hybrid system controls of natural ventilation and HVAC in mixed-mode buildings: A comprehensive review. *Energy and Buildings*, *276*, Article 112509.

Peng, L., Liu, J.-P., Wang, Y., Chan, P.-W., Lee, T.-C., Peng, F., Wong, M.-S., & Li, Y. (2018). Wind weakening in a dense high-rise city due to over nearly five decades of urbanization. *Building and Environment*, *138*, 207–220.

Peng, C., Ming, T., Gui, J., Tao, Y., & Peng, Z. (2015). Numerical analysis on the thermal environment of an old city district during urban renewal. *Energy and Buildings*, *89*, 18–31.

Percival, G. C. (2023). Heat tolerance of urban trees – A review. *Urban Forestry and Urban Greening*, *86*, Article 128021.

Priya, U. K., & Senthil, R. (2021). A review of the impact of the green landscape interventions on the urban microclimate of tropical areas. *Building and Environment*, *205*, Article 108190.

Qiu, C., Mou, L., Schmitt, M., & Zhu, X. X. (2019). Local climate zone-based urban land cover classification from multi-seasonal Sentinel-2 images with a recurrent residual network. *ISPRS Journal of Photogrammetry and Remote Sensing*, *154*, 151–162.

Raghu, D., Bucher, M. J. J., & De Wolf, C. (2023). Towards a 'resource cadastre' for a circular economy–urban-scale building material detection using street view imagery and computer vision. *Resources, Conservation and Recycling*, *198*, Article 107140.

Rahman, M. A., Moser, A., Gold, A., Rötzer, T., & Pauleit, S. (2018). Vertical air temperature gradients under the shade of two contrasting urban tree species during different types of summer days. *Science of the Total Environment*, *633*, 100–111.

Reyes-Riveros, R., Altamirano, A., De La Barrera, F., Rozas-Vásquez, D., Vieli, L., & Meli, P. (2021). Linking public urban green spaces and human well-being: A systematic review. *Urban Forestry and Urban Greening*, *61*, Article 127105.

Ricci, A., Guasco, M., Caboni, F., Orlanno, M., Giachetta, A., & Repetto, M. P. (2022). Impact of surrounding environments and vegetation on wind comfort assessment of a new tower with vertical green park. *Building and Environment*, *207*, Article 108409.

Saadi, I., Aganze, R., Moeinaddini, M., Asadi-Shekari, Z., & Cools, M. (2021). A participatory assessment of perceived neighbourhood walkability in a small urban environment. *Sustainability: Science, Practice and Policy*, *14*(1), 206.

Seiferling, I., Naik, N., Ratti, C., & Proulx, R. (2017). Green streets- Quantifying and mapping urban trees with street-level imagery and computer vision. *Landscape and Urban Planning*, *165*, 93–101.

Sharmin, T., Steemers, K., & Matzarakis, A. (2017). Microclimatic modelling in assessing the impact of urban geometry on urban thermal environment. *Sustainable Cities and Society*, *34*, 293–308.

Shartova, N. V., Mironova, E. E., & Grischenko, M. Y. (2023). Spatial disparities of street walkability in Moscow in the context of healthy urban environment. *Cities*, *141*, Article 104469.

Shi, Y., Ren, C., Zheng, Y., & Ng, E. (2016). Mapping the urban microclimatic spatial distribution in a sub-tropical high-density urban environment. *Architectural Science Review*, *59*(5), 370–384.

Shiflett, S. A., Liang, L. L., Crum, S. M., Feyisa, G. L., Wang, J., & Jenerette, G. D. (2017). Variation in the urban vegetation, surface temperature, air temperature nexus. *Science of the Total Environment*, *579*, 495–505.

Shijie, J., Ping, W., Peiyi, J., & Siping, H. (2017). Research on data augmentation for image classification based on convolution neural networks. In *2017 Chinese automation congress* CAC, (pp. 4165–4170). IEEE.

Steyn, D. G., Oke, T. R., Hay, J. E., & Knox, J. L. (1981). On scales in meteorology and climatology. *Climatological Bulletin*, *39*, 1–8.

Sun, H., Chen, Y., Li, K., & Gao, S. (2024). Spatio-temporal assessment of heat health risk in Chinese metropolitan cities based on the modified multi-indicators coupled risk framework. *Sustainable Cities and Society*, *108*, Article 105451.

Tabatabaei, S. S., & Fayaz, R. (2023). The effect of facade materials and coatings on urban heat island mitigation and outdoor thermal comfort in hot semi-arid climate. *Building and Environment*, *243*, Article 110701.

Taleghani, M., Marshall, A., Fitton, R., & Swan, W. (2019). Renaturing a microclimate: The impact of greening a neighbourhood on indoor thermal comfort during a heatwave in Manchester, UK. *Solar Energy*, *182*, 245–255.

Timilsina, S., Aryal, J., & Kirkpatrick, J. B. (2020). Mapping urban tree cover changes using object-based convolution neural network (OB-CNN). *Remote Sensing*, *12*(18), 3017.

Wang, C., Antos, S. E., & Triveno, L. M. (2021). Automatic detection of unreinforced masonry buildings from street view images using deep learning-based image segmentation. *Automation in Construction*, *132*, Article 103968.

Wang, X., Hsu, A., & Chakraborty, T. C. (2023). Citizen and machine learning-aided high-resolution mapping of urban heat exposure and stress. *Environmental Research: Infrastructure and Sustainability*, *3*(3), Article 035003.

Wang, D., Jin, M., Tong, D., Chang, X., Gong, Y., & Liu, Y. (2024). Evaluating the bikeability of urban streets using dockless shared bike trajectory data. *Sustainable Cities and Society*, *101*, Article 105181.

Wang, R., Liu, Y., Lu, Y., Zhang, J., Liu, P., Yao, Y., & Grekousis, G. (2019). Perceptions of built environment and health outcomes for older Chinese in Beijing: A big data approach with street view images and deep learning technique. *Computers, Environment and Urban Systems*, *78*, Article 101386.

Wang, W., Liu, K., Zhang, M., Shen, Y., Jing, R., & Xu, X. (2021). From simulation to data-driven approach: A framework of integrating urban morphology to low-energy urban design. *Renewable Energy*, *179*, 2016–2035.

Wang, C., Ren, Z., Guo, Y., Zhang, P., Hong, S., Ma, Z., Hong, W., & Wang, X. (2024). Assessing urban population exposure risk to extreme heat: Patterns, trends, and implications for climate resilience in China (2000–2020). *Sustainable Cities and Society*, *103*, Article 105260.

Wang, W., Xiao, L., Zhang, J., Yang, Y., Tian, P., Wang, H., & He, X. (2018). Potential of internet street-view images for measuring tree sizes in roadside forests. *Urban Forestry and Urban Greening*, *35*, 211–220.

Wang, J.-W., Yang, H.-J., & Kim, J.-J. (2020). Wind speed estimation in urban areas based on the relationships between background wind speeds and morphological parameters. *Journal of Wind Engineering and Industrial Aerodynamics*, *205*, Article 104324.

Weinberger, K. R., Zanobetti, A., Schwartz, J., & Wellenius, G. A. (2018). Effectiveness of national weather service heat alerts in preventing mortality in 20 US cities. *Environment International*, *116*, 30–38.

Wong, N. H., Tan, C. L., Nindyani, A. D. S., Jusuf, S. K., & Tan, E. (2012). Influence of water bodies on outdoor air temperature in hot and humid climate. In *ICSDC 2011* (pp. 81–89).

Wu, A. N., & Biljecki, F. (2021). Roofpedia: Automatic mapping of green and solar roofs for an open roofscape registry and evaluation of urban sustainability. *Landscape and Urban Planning*, *214*, Article 104167.

Xia, Y., Yabuki, N., & Fukuda, T. (2021). Sky view factor estimation from street view images based on semantic segmentation. *Urban Climate*, *40*, Article 100999.

Xiao, J., & Yuizono, T. (2022). Climate-adaptive landscape design: Microclimate and thermal comfort regulation of station square in the Hokuriku region, Japan. *Building and Environment*, *212*, Article 108813.

Xu, H., Chen, H., Zhou, X., Wu, Y., & Liu, Y. (2020). Research on the relationship between urban morphology and air temperature based on mobile measurement: A case study in Wuhan, China. *Urban Climate*, *34*, Article 100671.

Xu, L., Tong, S., He, W., Zhu, W., Mei, S., Cao, K., & Yuan, C. (2022). Better understanding on impact of microclimate information on building energy modelling performance for urban resilience. *Sustainable Cities and Society*, *80*, Article 103775.

Xu, Y., Vahmani, P., Jones, A., & Hong, T. (2024). Anthropogenic heat from buildings in Los Angeles county: A simulation framework and assessment. *Sustainable Cities and Society*, *107*, Article 105468.

Xu, F., Wong, M. S., Zhu, R., Heo, J., & Shi, G. (2023). Semantic segmentation of urban building surface materials using multi-scale contextual attention network. *ISPRS Journal of Photogrammetry and Remote Sensing*, *202*, 158–168.

Xu, Z., Zhang, F., Wu, Y., Yang, Y., & Wu, Y. (2023). Building height calculation for an urban area based on street view images and deep learning. *Computer-Aided Civil and Infrastructure Engineering*, *38*(7), 892–906.

Yamamoto, M., Ishida, Y., Mochida, A., Kobayashi, H., Watanabe, H., Abe, K., & Fujita, S. (2024). Assessment of cooling effect of sea breeze under future climate based on analysis of heat balance mechanism of urban space. *Building and Environment*, *253*, Article 111296.

Yan, B., Han, X., Malkawi, A., Dokka, T. H., Howard, P., Knowles, J., Hegli, T., & Edwards, K. (2022). Comprehensive assessment of operational performance of coupled natural ventilation and thermally active building system via an extensive sensor network. *Energy and Buildings*, *260*, Article 111921.

Yan, Y., & Huang, B. (2022). Estimation of building height using a single street view image via deep neural networks. *ISPRS Journal of Photogrammetry and Remote Sensing*, *192*, 83–98.

Yi, W., Chan, A. P. C., Wang, X., & Wang, J. (2016). Development of an early-warning system for site work in hot and humid environments: A case study. *Automation in Construction*, *62*, 101–113.

Yu, Z., Chen, S., Wong, N. H., Ignatius, M., Deng, J., He, Y., & Hii, D. J. C. (2020). Dependence between urban morphology and outdoor air temperature: A tropical campus study using random forests algorithm. *Sustainable Cities and Society*, *61*, Article 102200.

Yuan, J., Farnham, C., & Emura, K. (2021). Effect of different reflection directional characteristics of building facades on outdoor thermal environment and indoor heat loads by CFD analysis. *Urban Climate*, *38*, Article 100875.

Yuan, C., Norford, L., & Ng, E. (2017). A semi-empirical model for the effect of trees on the urban wind environment. *Landscape and Urban Planning*, *168*, 84–93.

Zeng, L., Lu, J., Li, W., & Li, Y. (2018). A fast approach for large-scale sky view factor estimation using street view images. *Building and Environment*, *135*, 74–84.

Zhang, J., Gou, Z., Zhang, F., & Shutter, L. (2020). A study of tree crown characteristics and their cooling effects in a subtropical city of Australia. *Ecological Engineering*, *158*, Article 106027.

Zhang, Z., Lv, Y., & Pan, H. (2013). Cooling and humidifying effect of plant communities in subtropical urban parks. *Urban Forestry and Urban Greening*, *12*(3), 323–329.

Zhang, W., & Zeng, H. (2024). Spatial differentiation characteristics and influencing factors of the Green View Index in urban areas based on street view images: A case study of Futian District, Shenzhen, China. *Urban Forestry and Urban Greening*, *93*, Article 128219.

Zhang, M., Zhang, X., Guo, S., Xu, X., Chen, J., & Wang, W. (2021). Urban micro-climate prediction through long short-term memory network with long-term monitoring for on-site building energy estimation. *Sustainable Cities and Society*, *74*, Article 103227.

Zhao, X., He, J., Luo, Y., & Li, Y. (2022). An analytical method to determine typical residential district models for predicting the urban heat island effect in residential areas. *Urban Climate*, *41*, Article 101007.

Zhao, T., Liang, X., Tu, W., Huang, Z., & Biljecki, F. (2023). Sensing urban soundscapes from street view imagery. *Computers, Environment and Urban Systems*, *99*, Article 101915.

Zhao, Q., Sailor, D. J., & Wentz, E. A. (2018). Impact of tree locations and arrangements on outdoor microclimates and human thermal comfort in an urban residential environment. *Urban Forestry and Urban Greening*, *32*, 81–91.

Zhong, Z., Zheng, L., Kang, G., Li, S., & Yang, Y. (2020). Random erasing data augmentation. *AAAI*, *34*(07), 13001–13008.

Zhou, H., He, S., Cai, Y., Wang, M., & Su, S. (2019). Social inequalities in neighborhood visual walkability: Using street view imagery and deep learning technologies to facilitate healthy city planning. *Sustainable Cities and Society*, *50*, Article 101605.

Zhou, X., Yamamoto, M., Yan, S., Ishida, Y., Cai, M., Ji, Q., Makvandi, M., & Li, C. (2022). Exploring the impacts of heat release of vehicles on urban heat mitigation in Sendai, Japan using WRF model integrated with urban LCZ. *Sustainable Cities and Society*, *82*, Article 103922.